CrossMark

*J. Fluid Mech.* (2017), *vol.* 832, *pp.* 5–40. © Cambridge University Press 2017
doi:10.1017/jfm.2017.680



# Lagrangian transport in a class of three-dimensional buoyancy-driven flows

**P. S. Contreras[1,2], M. F. M. Speetjens[1,†] and H. J. H. Clercx[2]**

[1]Energy Technology Laboratory, Department of Mechanical Engineering, Eindhoven University of Technology, P.O. Box 513, 5600 MB Eindhoven, The Netherlands

[2]Fluid Dynamics Laboratory, Department of Applied Physics, Eindhoven University of Technology, P.O. Box 513, 5600 MB Eindhoven, The Netherlands

(Received 14 February 2017; revised 13 July 2017; accepted 19 September 2017; first published online 26 October 2017)

The present study concerns the Lagrangian dynamics of three-dimensional (3D) buoyancy-driven cavity flows under steady and laminar conditions due to a global temperature gradient imposed via an opposite hot and cold sidewall. This serves as the archetypal configuration for natural-convection flows in which (contrary to the well-known Rayleigh–Bénard flow) gravity is perpendicular (instead of parallel) to the global temperature gradient. Limited insight into the Lagrangian properties of this class of flows, despite its relevance to observed flow phenomena as well as scalar transport, motivates this study. The 3D Lagrangian dynamics are investigated in terms of the generic structure and associated transport properties of the global streamline pattern ('Lagrangian flow topology') by both theoretical and computational analyses. The Grashof number $Gr$ is the principal control parameter for the flow topology: limit $Gr = 0$ yields a trivial state of closed streamlines; $Gr > 0$ induces symmetry breaking by fluid inertia and buoyancy and thus causes formation of toroidal coherent structures ('primary tori') embedded in chaotic streamlines governed by Hamiltonian mechanisms. Fluid inertia prevails for 'smaller' $Gr$ and gives behaviour that is dynamically entirely analogous to 3D lid-driven cavity flows. Buoyancy-induced bifurcation of the flow topology occurs for 'larger' $Gr$ and underlies the emergence of 'secondary rolls' observed in the literature and to date unreported secondary tori for 'larger' Prandtl numbers $Pr$. Key to these dynamics are stagnation points and corresponding heteroclinic manifold interactions.

**Key words:** chaotic advection, convection in cavities, topological fluid dynamics

## 1. Introduction

Fluid flow driven by buoyancy due to natural convection is relevant in many flow systems in nature, industry and technical applications (Turcotte & Schubert 2002; Nield & Bejan 2006; Giaiotti, Steinacker & Stel 2007; Awbi 2008; Davies 2011; Bejan 2013). An archetypal configuration for studying the fundamentals of such

†Email address for correspondence: m.f.m.speetjens@tue.nl

https://doi.org/10.1017/jfm.2017.680 Published online by Cambridge University Press

systems exists in a flow inside a rectangular cavity driven by buoyancy due to a global temperature gradient imposed via a hot bottom and cold top wall. This gives rise to the well-known Rayleigh–Bénard convection that has been the subject of investigation in a large body of work in a fluid-dynamical context as well as in the broader scope of nonlinear dynamics (Getling 1998; Lappa 2010). Buoyancy-driven cavity flow due to a global temperature gradient imposed via an opposite hot and cold sidewall has gradually emerged as a complementary problem to the Rayleigh–Bénard case (Lappa 2010). This configuration is relevant to the buoyancy-induced onset of unsteadiness and turbulence as well as a range of (industrial) applications (de Vahl Davis 1983; Phillips 1984; Mercader *et al.* 2005; Lappa 2010; Oteski, Duguet & Pastur 2014; Oteski *et al.* 2015). Moreover, it is well-suited as a benchmark for computational algorithms for natural-convection flows (Wakashima & Saitoh 2004; Bennett, Anne & Hsueh 2006). The principal difference between the Rayleigh–Bénard and side-heated problems is that gravity is parallel and perpendicular to the global temperature gradient in the former and latter system, respectively, which dramatically changes the dynamics (Lappa 2010). Hence, both systems capture different fundamental aspects of natural-convection flows. (Consider to this end the hydrostatic balance of a fluid at rest, implying a pressure gradient parallel to gravity ($\boldsymbol{\nabla} p = \rho \boldsymbol{g} \propto \boldsymbol{g}$), and a temperature-dependent density $\rho = \rho(T)$. The well-known baroclinic vector $\boldsymbol{b} = \boldsymbol{\nabla} p \times \boldsymbol{\nabla} \rho$ is the sole vorticity source for a still fluid and thus offers insight into the mechanisms behind incipient fluid motion. Temperature gradients parallel with gravity ($\boldsymbol{\nabla} T \propto \boldsymbol{g}$) via $\boldsymbol{\nabla} \rho = (\mathrm{d}\rho/\mathrm{d}T)\boldsymbol{\nabla} T \propto \boldsymbol{g}$ imply a barotropic state ($\boldsymbol{b} \propto \boldsymbol{g} \times \boldsymbol{g} = \boldsymbol{0}$); non-parallel temperature gradients via $\boldsymbol{\nabla} \rho = (\mathrm{d}\rho/\mathrm{d}T)\boldsymbol{\nabla} T \not\propto \boldsymbol{g}$ imply a baroclinic state ($\boldsymbol{b} \not\propto \boldsymbol{0}$). Thus non-zero temperature gradients in the non-parallel case immediately set the fluid in motion through vorticity production; the parallel case, on the other hand, lacks such a mechanism and may remain at rest for non-zero temperature gradients (explaining why Rayleigh–Bénard convection requires a minimum temperature drop). Hence, systems with parallel and non-parallel temperature gradients are fundamentally different.) However, despite its relevance, the side-heated configuration has nonetheless received far less attention than the Rayleigh–Bénard case. This motivates the present study on the side-heated system (denoted 'buoyancy-driven (cavity) flow' hereafter).

Studies on buoyancy-driven cavity flows predominantly concentrate on (nonlinear) behaviour of the Eulerian flow field such as, for example, onset of fluid motion, bifurcations in the spatial structure of velocity and vorticity fields (e.g. formation of 'eddies' and 'rolls') and transitions from steady to unsteady flows. Pioneering work is found in Batchelor (1954), Elder (1965), Gill (1966), Ostrach (1972) and earlier studies on a range of enclosures are reviewed in Ostrach (1988). Lappa (2010) gives a comprehensive survey of later and recent studies. Lagrangian properties are to date mainly investigated phenomenologically within an otherwise Eulerian study by, for example, inferring the existence of toroidal structures from spiralling streamlines (Mallinson & de Vahl Davis 1977; Henry & Buffat 1998; Melnikov & Shevtsova 2005) and demonstrating global bifurcations by way of streamline portraits (Mallinson & de Vahl Davis 1977; Hiller, Koch & Kowalewski 1989; Yarin *et al.* 1996). Dedicated Lagrangian analyses, on the other hand, are scarce, despite their relevance for understanding aspects ranging from the above-mentioned observations on streamlines to (chaotic) scalar transport in fluid systems (Metcalfe *et al.* 2012; Aref *et al.* 2017). Chaotic advection in two-dimensional (2D) unsteady buoyancy-driven flows and associated Lagrangian entities as periodic points and manifolds are, for example, investigated in Mercader *et al.* (2005), Oteski *et al.* (2014), Oteski *et al.* (2015); essentially three-dimensional (3D) Lagrangian studies are, to the best of our

https://doi.org/10.1017/jfm.2017.680 Published online by Cambridge University Press

knowledge, restricted to Hiller *et al.* (1989), Sheu *et al.* (2008) on the 3D manifold topology of stagnation points and Contreras, de la Cruz & Ramos (2016*a*), Contreras, Speetjens & Clercx (2016*b*) on 3D chaotic advection and corresponding entities as invariant surfaces and periodic lines in steady and time-periodic flows. However, notwithstanding these efforts, insight into Lagrangian transport (particularly in 3D) buoyancy-driven flows remains limited.

The present study addresses the above matter by an in-depth Lagrangian analysis of the global streamline pattern ('Lagrangian flow topology') in 3D buoyancy-driven flows in a cubical cavity under steady and laminar conditions. (Rayleigh numbers are well below the onset of unsteadiness (Henkes & Hoogendoorn 1990) so as to ensure steady and laminar flow.) This expands on Contreras *et al.* (2016*a*,*b*), and embarks on the introduction of a non-dimensional parameterisation that (contrary to the standard approach) admits smooth introduction of nonlinearities in the Lagrangian dynamics due to fluid inertia and/or convective heat transfer. Symmetry analysis establishes the link conjectured in Contreras *et al.* (2016*a*,*b*) of buoyancy-driven flows with the dynamically/topologically analogous class of lid-driven cavity flows inside cubical or cylindrical domains (Shankar & Deshpande 2000; Speetjens & Clercx 2013). This implies two fundamental similarities between both flow classes: (i) diffeomorphic Lagrangian flow topologies (at least under weakly nonlinear conditions); (ii) a (locally) Hamiltonian structure of the 3D Lagrangian equations of motion. These similarities pave the way to the present in-depth Lagrangian analysis of the 3D steady buoyancy-driven flow by methods from Hamiltonian mechanics and nonlinear dynamics.

Insight into the Lagrangian dynamics of 3D steady cavity flows is also relevant for the important class of time-periodic cavity flows composed of reoriented steady flows (Aref *et al.* 2017). Certain Lagrangian phenomena of time-periodic lid-driven cylinder flows, for example, intimately relate to that of the underlying steady flows (Speetjens & Clercx 2013); a first similar study on time-periodic buoyancy-driven flows is in Contreras *et al.* (2016*a*).

This article is organised as follows. The mathematical model and numerical methods are introduced in § 2. The generic structure of the Lagrangian flow topology and the associated transport properties are discussed in § 3. This is further elaborated in § 4 by distinction of inertia-dominated versus thermo-inertial flows (i.e. driven by an interplay of fluid inertia and buoyancy). The intricate 3D flow topologies in the thermo-inertial regime are demonstrated and examined in § 5. Conclusions are given in § 6.

## 2. Problem definition

### 2.1. *Flow model and tracer kinematics*

We consider the steady flow inside a cubical cavity (side length $H$) driven by buoyancy due to differential heating by two opposite vertical sidewalls at different temperature. The origin of the frame of reference is located in a corner of the cavity and gravity acts in the negative $z$-direction as per figure 1. The fluid motion is driven by differential heating via the cold vertical wall at $x = 0$ (temperature $T_0 < T_{bulk}$) and the hot vertical wall $x = H$ (temperature $T_1 > T_{bulk}$); the other walls are thermally insulated ($\partial T/\partial n = 0$, with $n$ the wall normal). This sets up a circulatory flow due to rising and descending fluid at the hot and cold walls, respectively, as indicated schematically in figure 1. Furthermore, all walls are rigid and stationary, imposing no-slip conditions on the velocity ($\boldsymbol{u} = \boldsymbol{0}$).

https://doi.org/10.1017/jfm.2017.680 Published online by Cambridge University Press

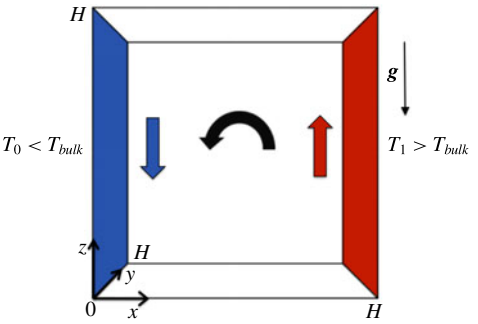



FIGURE 1. (Colour online) Buoyancy-driven flow inside a cubical cavity due to differential heating via cold (blue; temperature $T_0 < T_{bulk}$) and hot (red; $T_1 > T_{bulk}$) vertical walls (perspective view into 3D cavity along $y$-axis). Other walls are thermally insulated. This sets up circulatory flow (black arrow) due to rising (red arrow) and descending (blue arrow) fluid at hot and cold walls, respectively.

A Newtonian fluid with a velocity $\boldsymbol{u}$ governed by the steady Boussinesq equations

$$\boldsymbol{\nabla}\cdot\boldsymbol{u}=0,\quad \rho\boldsymbol{u}\cdot\boldsymbol{\nabla}\boldsymbol{u}=-\boldsymbol{\nabla}p+\mu\nabla^2\boldsymbol{u}+\rho\beta g(T-T_{ref})\boldsymbol{e}_z,\quad \boldsymbol{u}\cdot\boldsymbol{\nabla}T=\alpha\nabla^2T,\quad (2.1a{-}c)$$

is assumed, where $T$, $p$ and $\rho$ are temperature, pressure and density, respectively, $T_{ref}$ the reference temperature for the fluid properties (here $T_{ref}=T_0$), $g$ the gravitational acceleration, $\boldsymbol{e}_z$ the $z$-wise unit vector, $\mu$ the dynamic viscosity, $\beta$ the thermal expansion coefficient and $\alpha$ the thermal diffusivity (Bird, Stewart & Lightfoot 2007; Lappa 2010).

The Lagrangian motion of tracers passively advected by the velocity field $\boldsymbol{u}$ is governed by the kinematic equation and its corresponding (formal) solution

$$\frac{\mathrm{d}\boldsymbol{x}}{\mathrm{d}t}=\boldsymbol{u}(\boldsymbol{x}),\quad \boldsymbol{x}(t)=\boldsymbol{\Phi}_t(\boldsymbol{x}_0),\qquad (2.2a,b)$$

with $\boldsymbol{x}(t)$ and $\boldsymbol{x}_0$ the current and initial tracer positions, respectively, and $\boldsymbol{\Phi}_t$ the corresponding flow (Aref 2002). Curves $\boldsymbol{x}(t)$ parameterised by $t$ describe the Lagrangian fluid trajectories, and in the current steady case coincide with the streamlines of the flow.

### 2.2. *Non-dimensional formulation*

The problem defined above will for reasons of universality be investigated in non-dimensional form. Non-dimensionalisation relies the scaling $\boldsymbol{x}=H\boldsymbol{x}'$, $\boldsymbol{u}=U\boldsymbol{u}'$, $p=Pp'$ and $T=T_0+\Delta TT'$, with $U=g\beta\Delta TH^2/\nu$, $P=\mu U/H$, $H$ as before and $\Delta T=T_1-T_0$ the global temperature drop. Substitution in (2.1) and rearrangement (after dropping primes) yields

$$\boldsymbol{\nabla}\cdot\boldsymbol{u}=0,\quad Gr\boldsymbol{u}\cdot\boldsymbol{\nabla}\boldsymbol{u}=-\boldsymbol{\nabla}p+\nabla^2\boldsymbol{u}+T\boldsymbol{e}_z,\quad GrPr\boldsymbol{u}\cdot\boldsymbol{\nabla}T=\nabla^2T,\quad (2.3a{-}c)$$

as non-dimensional Boussinesq approximation, parameterised by the Prandtl number $Pr=\nu/\alpha$ and Grashof number $Gr=g\beta\Delta TH^3/\nu^2$, where $\nu=\mu/\rho$ is the kinematic viscosity. Thus the problem translates into a differentially heated cavity with unit side length and thermal boundary conditions $T=0$ at $x=0$ and $T=1$ at $x=1$.

https://doi.org/10.1017/jfm.2017.680 Published online by Cambridge University Press

Non-dimensional form (2.3) concerns specifically the present regime of interest, *viz.* steady buoyancy-driven flow at strongly laminar conditions, implying a flow dominated by a balance between buoyancy (driving force) and viscous friction (restoring force), and thus the above characteristic velocity $U$ (Ostrach 1988). This flow regime, given $Gr = UH/\nu = Re$ (Reynolds number), typically restricts the system to 'lower' $Gr$.

The non-dimensional kinematic equation follows from scaling time as $t = \tau t'$, with $\tau = H/U$ the advective time scale, yielding a form identical to (2.2).

### 2.3. *Numerical methods*

The velocity and temperature fields governed by (2.3) were simulated by the commercial CFD package `COMSOL Multiphysics` using the `Laminar Flow` and `Heat Transfer in Fluids` modules with standard settings. The computational mesh consisted of $O(10^5)$ elements and employed mesh refinement near the isothermal walls ($x = 0, 1$). The tolerance factor for the nonlinear solver was set to yield residuals of $O(10^{-10} - 10^{-12})$.

The Lagrangian fluid trajectories are determined by numerical integration of the kinematic equation (2.2) using an explicit third-order Taylor–Galerkin (TG) scheme with adaptive step size (Speetjens, Clercx & van Heijst 2006; Moharana *et al.* 2013). Critical for reliable Lagrangian tracking is accurate approximation of the incompressibility constraint $\boldsymbol{\nabla} \cdot \boldsymbol{u} = 0$ at any position $\boldsymbol{x}$ in the flow domain. However, the degree of accuracy of commercial CFD packages in combination with the typical error propagation of standard spatial interpolation schemes for evaluation of the velocity in arbitrary positions generically introduces departures from incompressibility that may lead to numerical artefacts in the Lagrangian fluid trajectories. Thus an approach that ensures accurate approximation of the incompressibility constraint at any position $\boldsymbol{x}$ is essential. Consider to this end the dramatic difference in performance of the above TG scheme using standard interpolation of the velocity field of a typical commercial flow solver versus a dedicated flow solver and interpolation scheme for Lagrangian analyses based on a high-precision spectral method (Speetjens & Clercx 2005). The present study adopts a similar spectral approach by projection of the `COMSOL` field onto a divergence-free basis constructed from Chebyshev polynomials according to the method in § A.1. Performance of the TG tracking scheme using this spectral representation of the velocity field is evaluated in § A.2 and reveals reliable simulation of the Lagrangian dynamics.

## 3. Lagrangian dynamics

### 3.1. *Fundamental states of the Lagrangian flow topology*

Non-dimensional form (2.3) admits identification of two fundamental flow states that are relevant in the context of the transport phenomena.

(i) *Limit* $Gr = 0$. Here system (2.3) collapses on the linear Stokes limit $-\boldsymbol{\nabla} p + \boldsymbol{\nabla}^2 \boldsymbol{u} + T\boldsymbol{e}_z = 0$ and the conductive limit $\boldsymbol{\nabla}^2 T = 0$.

(ii) *General case* $Gr > 0$. The convective terms in the momentum and energy balances become relevant and render the system essentially nonlinear.

Figure 2 illustrates the essential features of both states in terms of temperature field and typical streamlines for $Pr = 0.71$. Figure 2(*a–c*) demonstrate the convergence

https://doi.org/10.1017/jfm.2017.680 Published online by Cambridge University Press

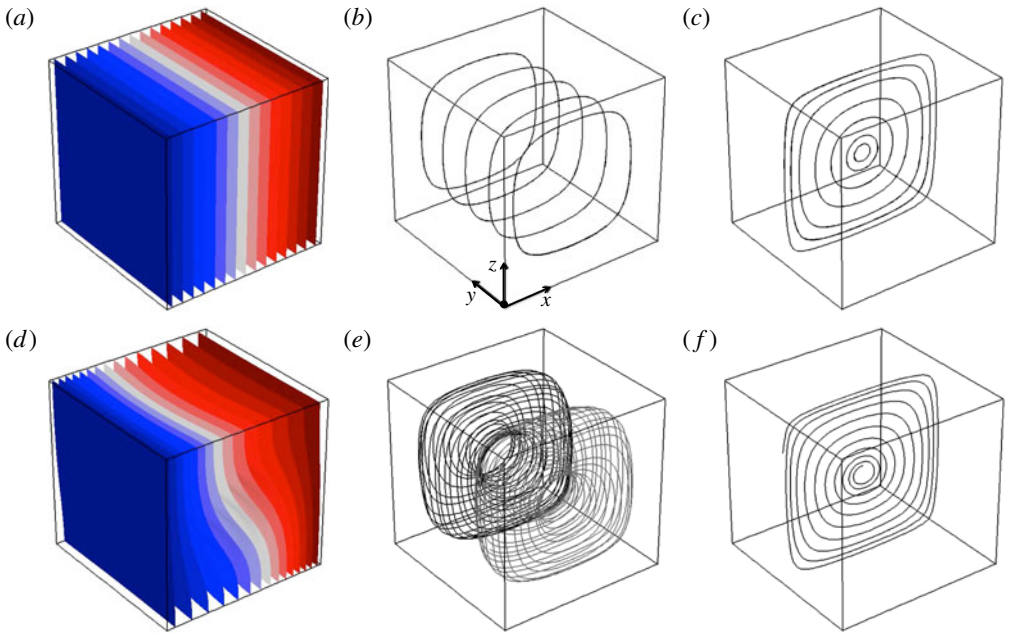



FIGURE 2. (Colour online) Temperature field ($a$,$d$) and typical streamlines ($b$,$e$, $c$,$f$) in limit $Gr = 0$ ($a$–$c$) versus general case $Gr > 0$ ($d$–$f$; $Gr = 3.2 \times 10^3$) demonstrated for $Pr = 0.71$. Blue/red in ($a$,$d$) indicates minimum/maximum temperatures; ($c$,$f$) gives streamlines in midplane $y = 1/2$. The dot in panel ($b$) indicates the origin of the shown reference frame.

on a linear temperature field and closed streamlines for vanishing $Gr$. Here fluid motion consists solely of a primary circulation along these streamlines. Figure 2($d$–$f$) demonstrate the essentially nonlinear temperature field and non-closed streamlines associated with departures from the limit $Gr = 0$ by way of $Gr = 3.2 \times 10^3$. Streamlines outside midplane $y = 1/2$ describe toroidal structures as shown in figure 2($e$) and cause fluid parcels, besides said primary circulation, to perform an additional secondary circulation about the common centre (not shown) of these tori; the streamlines in the midplane emerge from a central stagnation point (not shown) and spiral outward towards the cavity walls (figure 2$f$). The behaviour of this stagnation point is key to the global Lagrangian dynamics and is investigated in detail in § 4.3. Moreover, the generic emergence of the above topological states as a function of $Gr$ is inextricably linked to symmetry properties and the Hamiltonian structure of the Lagrangian equations of motion. The former and latter will be investigated in §§ 3.2 and 3.4, respectively.

The above transition from linear temperature distributions and closed streamlines to nonlinear temperature fields and toroidal structures upon increasing $Gr$ from the limit $Gr = 0$ is generic for any fluid and thus (qualitatively) independent of $Pr$ here. However, in order to nonetheless explore the (quantitative) role of $Pr$, the Lagrangian dynamics in buoyancy-driven flows is in the present study demonstrated and investigated mainly by way of two specific cases, *viz.* air ($Pr = 0.71$) and water ($Pr = 7$). This is motivated by their great practical relevance and prominence in the literature (de Vahl Davis 1983; Melnikov & Shevtsova 2005; Lappa 2010; Oteski *et al.* 2015; Contreras *et al.* 2016*b*).

https://doi.org/10.1017/jfm.2017.680 Published online by Cambridge University Press

### 3.2. *Symmetry analysis*

Symmetries are key organising mechanisms of the Lagrangian flow topology and typically originate from an interplay between symmetries in geometry and governing equations (Laure 1987; Franjione & Ottino 1992; Speetjens, Clercx & van Heijst 2004; Speetjens *et al.* 2014). Relevant in the present context is that the buoyancy term in the momentum equation admits a Helmholtz decomposition (Arfken & Weber 2005) into an irrotational and solenoidal part as $\widetilde{T}\boldsymbol{e}_z = \boldsymbol{\nabla}\phi + \boldsymbol{\nabla}\times\boldsymbol{b}$, with $\boldsymbol{\nabla}\phi = \widetilde{T}\boldsymbol{e}_z$ and $\boldsymbol{\nabla}\times\boldsymbol{b} = \widehat{T}\boldsymbol{e}_z$, where $\widetilde{T} = 1/2$ and $\widehat{T} = T - 1/2$. (Note that $-1/2 \leqslant \widehat{T} \leqslant 1/2$.) This gives $\phi = z/2$, which merely adjusts the pressure (i.e. $p \to \widehat{p} = p - \phi$ in (2.3)), exposing $\widehat{T}\boldsymbol{e}_z$ as the effective buoyancy force.

Velocity $\boldsymbol{u}$ and temperature contribution $\widehat{T}$ possess the following symmetries for buoyancy-driven flow in rectangular cavities in the general case $Gr > 0$ (Laure 1987).

(i) Reflectional symmetry about plane $y = 1/2$ (denoted $\mathcal{P}$ hereafter):

$$\boldsymbol{S}_i : (x, y, z) \to (x, 1-y, z), \quad (u_x, u_y, u_z, \widehat{T}) \to (u_x, -u_y, u_z, \widehat{T}). \tag{3.1a,b}$$

(ii) Centro-symmetry about line $x = z = 1/2$ (denoted $\mathcal{L}$ hereafter):

$$\boldsymbol{S}_{ii} : (x, y, z) \to (1-x, y, 1-z), \quad (u_x, u_y, u_z, \widehat{T}) \to (-u_x, u_y, -u_z, -\widehat{T}). \tag{3.2a,b}$$

Numerous computational studies confirm symmetries (3.1) and (3.2) (Labrosse *et al.* 1997; Henry & Buffat 1998; Juel *et al.* 1999; Wakashima & Saitoh 2004; Bennett *et al.* 2006; Henry *et al.* 2008).

Centro-symmetry (3.2) in the limit $Gr = 0$ divides into the reflectional symmetry

$$\boldsymbol{S}_{ii,x} : (x, y, z) \to (1-x, y, z), \quad (u_x, u_y, u_z, \widehat{T}) \to (u_x, -u_y, -u_z, -\widehat{T}), \tag{3.3a,b}$$

about plane $x = 1/2$ and the reflectional symmetry

$$\boldsymbol{S}_{ii,z} : (x, y, z) \to (x, y, 1-z), \quad (u_x, u_y, u_z, \widehat{T}) \to (-u_x, -u_y, u_z, \widehat{T}), \tag{3.4a,b}$$

about plane $z = 1/2$. Note that the symmetries relate via $\boldsymbol{S}_{ii} = \boldsymbol{S}_{ii,x}\boldsymbol{S}_{ii,z} = \boldsymbol{S}_{ii,z}\boldsymbol{S}_{ii,x}$. Symmetries (3.3) and (3.4) emerge on grounds of vanishing inertial and convective terms in (2.3) in the limit $Gr = 0$. Inertia and/or convective heat transfer induced by appreciable $Gr > 0$ breaks these symmetries in favour of symmetry (3.2). Hence, cases $Gr = 0$ and $Gr > 0$ are essentially distinct and underlie the fundamental topological states identified in § 3.1. This is elaborated below.

Symmetry (3.1), commonly denoted 'left–right symmetry' in convection problems, exists for any $Gr$ and separates the domain into two subregions by $\mathcal{P}$. The latter, since $u_y = 0$ due to the anti-symmetry of $u_y$, constitutes an invariant material plane bounded by the cavity walls. This has two immediate topological consequences. First, Lagrangian entities are either restricted to $\mathcal{P}$ or emerge as symmetric pairs about this plane. Second, midplane $\mathcal{P}$ must, by virtue of Brouwer's fixed-point theorem (Brouwer 1911), hold at least one stagnation point $\boldsymbol{u} = \boldsymbol{0}$.

The fundamental flow states of § 3.1 emanate from the above symmetries as follows.

(i) *Limit* $Gr = 0$. The primary circulation causes streamlines to generically cross the symmetry plane $x = 1/2$ of reflectional symmetry (3.3). (This ignores possible corner eddies (Shankar 1997); these are very weak and highly localised and

https://doi.org/10.1017/jfm.2017.680 Published online by Cambridge University Press

thus irrelevant to the overall Lagrangian dynamics.) This has the fundamental implication that such streamlines must be closed (Shankar 1997). Note that symmetry (3.4) has the same effect. Moreover, interaction of symmetries (3.1), (3.3) and (3.4) results in the formation of a stagnation line $x = z = 1/2$. Hence, the Lagrangian flow topology generically consists of closed streamlines centred on said stagnation line that individually exhibit reflectional symmetry about both planes $x = 1/2$ and $z = 1/2$ and emerge in symmetric pairs about $\mathcal{P}$ (as demonstrated in figure 2*b*).

(ii) *General case* $Gr > 0$. Breakdown of reflectional symmetries (3.3) and (3.4) in favour of centro-symmetry (3.2) eliminates the constraining mechanism underlying the formation of closed streamlines. Hence, streamlines generically become non-closed in this regime. Moreover, the stagnation line gives way to an isolated stagnation point $\boldsymbol{x}_c = (1/2, 1/2, 1/2)$ in the centre of the cavity, which results from the interaction of symmetries (3.1) and (3.2). Thus the Lagrangian flow topology generically consists of non-closed streamlines that each describe toroidal structures arranged symmetrically about $\mathcal{P}$ in the way demonstrated in figure 2(*e*). Figure 3 gives the corresponding intersections with plane $x = 1/2$ for $Gr = 7.9 \times 10^2$ and thus exposes these toroidal structures. Note that $\boldsymbol{S}_{ii}$ implies a reflectional symmetry about lines $z = 1/2$ and $x = 1/2$ within the planes $x = 1/2$ and $z = 1/2$, respectively. This causes the symmetry of shown cross-sections with plane $x = 1/2$ about both lines $y = 1/2$ and $z = 1/2$ (dashed in figure 3) and a similar symmetry in plane $z = 1/2$ about lines $x = 1/2$ and $y = 1/2$.

The above rigorously links the generic topological make-up of the 3D streamline portrait to symmetries, which is key to the present study. Symmetries namely 'shape' the fundamental topological states identified in § 3.1. Moreover, the particular way in which symmetries are broken dictates the response of the flow topology and, inherently, the Lagrangian transport properties to perturbations. Symmetry and symmetry breaking (investigated in § 4) are controlled primarily by the Grashof number $Gr$, and thus underscores the crucial role of this parameter for the Lagrangian dynamics.

### 3.3. *Topological equivalence with single-wall lid-driven cavity flows*

The above symmetries establish a fundamental link between the buoyancy-driven flow and lid-driven cavity flows. Fluid motion in cylindrical or cubical domains driven by a single endwall $z = 0$ or $z = H$ in the Stokes limit ($Re = 0$) namely possess the same symmetries (3.1) and (3.3) and, in consequence, their flow topology also consists of closed streamlines centred on a stagnation line symmetric about $\mathcal{P}$ similar to in figure 2(*b*) (Shankar 1997; Shankar & Deshpande 2000; Speetjens *et al.* 2004). A counterpart to symmetry (3.4) is absent in single-wall lid-driven Stokes flows ($Re = 0$) yet this is, other than admitting asymmetry about the plane $z = 1/2$, inconsequential for the topological equivalence with the buoyancy-driven flow (limit $Gr = 0$). The equivalence extends to lid-driven flows with fluid inertia ($Re > 0$) in that, similar to case $Gr > 0$, symmetry (3.3) is broken, causing streamlines to generically become non-closed and describe toroidal structures similar to in figure 2(*e*) (Shankar & Deshpande 2000; Speetjens *et al.* 2006; Speetjens & Clercx 2013). Absence of a counterpart to centro-symmetry (3.2) is again immaterial for the topological equivalence. Note that buoyancy-induced topological bifurcations may complicate (yet not eliminate) the equivalence (§ 4).

https://doi.org/10.1017/jfm.2017.680 Published online by Cambridge University Press

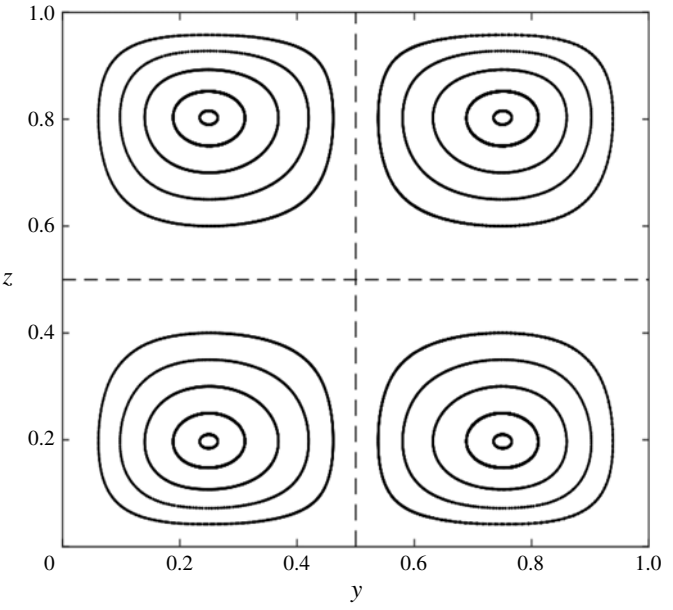



FIGURE 3. Formation of toroidal structures by non-closed streamlines in the generic case $Gr > 0$ demonstrated for $Gr = 7.9 \times 10^2$ and $Pr = 0.71$. Shown are cross-sections with the plane $x = 1/2$; these are always symmetric about lines $y = 1/2$ and $z = 1/2$ (dashed).

The topological equivalence between buoyancy-driven and lid-driven cavity flows implies a second fundamental link for these flow classes: the Lagrangian equations of motion (2.2) have a Hamiltonian structure. This has the important consequence that the response of the flow topology to departures from limit $Gr = 0$ is governed by the same universal Hamiltonian mechanisms as in single-wall lid-driven flows. The Hamiltonian structure and its ramifications for the Lagrangian dynamics are elaborated below.

### 3.4. *Formation of the flow topology by Hamiltonian mechanisms*

The primary circulation causes (similar to lid-driven flows) systematic return of generic streamlines to plane $x = 1/2$. This admits representation of the 3D flow $\boldsymbol{x}(t) = \boldsymbol{\Phi}_t(\boldsymbol{x}_0)$ governed by kinematic equation (2.2) by a 2D map $\boldsymbol{\Phi}$ within plane $x = 1/2$ according to

$$\boldsymbol{x}_{k+1} = \boldsymbol{\Phi}(\boldsymbol{x}_k), \tag{3.5}$$

with $\boldsymbol{x}_k = (y_k, z_k)$ the $k$th intersection of a 3D streamline originating from $\boldsymbol{x}_0$ with said plane (appendix B). The sequence of planar positions of a given fluid parcel, i.e.

$$\mathcal{X}(\boldsymbol{x}_0) = \{\boldsymbol{x}_0, \boldsymbol{x}_1, \ldots, \boldsymbol{x}_k, \ldots\}, \tag{3.6}$$

represents the subsequent intersections of its corresponding 3D streamline with plane $x = 1/2$ and constitutes its so-called Poincaré section. Coherent structures in the Poincaré section are inextricably linked to those in the 3D streamline portrait. Closed streamlines, for example, emerge as periodic points $\boldsymbol{\Phi}^p(\boldsymbol{x}_0) = \boldsymbol{x}_0$, with $p$ the

https://doi.org/10.1017/jfm.2017.680 Published online by Cambridge University Press

winding number of the streamline, in the corresponding Poincaré section. Similarly, 3D toroidal structures appear as 'islands' centred on periodic points in these sections; figure 3, for example, shows the Poincaré section of such tori for $Gr = 7.9 \times 10^2$ and $Pr = 0.71$ (which are similar to those in figure 2*e*). Thus map $\boldsymbol{\Phi}$ enables investigation of the flow topology both in terms of the dynamics within plane $x = 1/2$ and 3D streamlines.

Map $\boldsymbol{\Phi}$, in turn, through a suitable transformation from physical $(y, z)$ to canonical $(\zeta_1, \zeta_2)$ space coincides with a 2D Hamiltonian system, i.e.

$$\boldsymbol{x}_{k+1} = \boldsymbol{\Phi}(\boldsymbol{x}_k) \quad \Leftrightarrow \quad \left(\frac{\mathrm{d}\zeta_1}{\mathrm{d}\tau}, \frac{\mathrm{d}\zeta_2}{\mathrm{d}\tau}\right) = \left(\frac{\partial \mathcal{H}}{\partial \zeta_2}, -\frac{\partial \mathcal{H}}{\partial \zeta_1}\right), \tag{3.7}$$

with $\mathcal{H}$ the Hamiltonian. This ties the Lagrangian dynamics in plane $x = 1/2$ described by map (3.5) with 'snapshots' in canonical time $\tau$ of the Hamiltonian flow in canonical space $(\zeta_1, \zeta_2)$. Consult appendix B for technical details.

The link with Hamiltonian systems established above implies that the flow topology is governed by Hamiltonian mechanics. The behaviour of Hamiltonian systems emanates from the perturbation of the so-called integrable states (in essence states with fully regular dynamics along closed trajectories in phase space) (Ott 2002). For the present buoyancy-driven flows, the integrable state corresponds to the closed streamlines in the limit $Gr = 0$ (as, for example, in figure 2*b*). Perturbation by $Gr > 0$ admits non-closed streamlines and thus sets the stage for non-trivial flow topologies (including chaotic dynamics). The onset of such flow topologies is governed by well-defined Hamiltonian scenarios and is here (qualitatively) controlled by the Grashof number $Gr$ as follows.

(i) *Limit* $Gr = 0$. The underlying Hamiltonian system (3.7) assumes the integrable state, meaning its Hamiltonian becomes $\mathcal{H}(\zeta_1, \zeta_2, \tau) = C$, with $C$ an arbitrary constant. Thus each individual position in the associated Poincaré section constitutes a period-1 point, i.e. $\boldsymbol{\Phi}(\boldsymbol{x}_k) = \boldsymbol{x}_k$, consistent with the situation of all streamlines being individually closed (e.g. figure 2*b*). This state in fact is a singular limit in that it breaks down for any non-zero perturbation (Cartwright, Feingold & Piro 1996). (Limit $Gr = 0$ is singular also in the sense of implying vanishing dimensional flow due to scaling $U = Gr\nu/H$ ($= 0$ here). However, the corresponding non-dimensional flow is non-trivial and constitutes a non-inertial fluid driven by a symmetric buoyancy term resulting from a linear temperature profile governed by conductive heat transfer only. Hence, case $Gr = 0$, though strictly with trivial dimensional counterpart, is nonetheless relevant in the current Lagrangian context as the (theoretical) limit of fully integrable Lagrangian dynamics.)

(ii) *'Small' Gr*. Minute (non-zero) perturbations of $O(\epsilon)$, with $\epsilon \ll 1$, cause the Hamiltonian to become non-trivial yet remain independent of the canonical time $\tau$: $\mathcal{H} = \mathcal{H}(\zeta_1, \zeta_2)$ (Cartwright *et al.* 1996). ('Small' and 'large' $Gr$ are distinguished by the corresponding typical perturbation $\epsilon$.) This defines an autonomous 2D Hamiltonian system with Lagrangian motion (in bounded flows) restricted to concentric closed level sets of $\mathcal{H}$ in the Poincaré section (e.g. the islands in figure 3). These level sets underlie the nested tori that form in the 3D streamline portrait (e.g. figure 2*e*). The $\tau$-dependence vanishes due to the fact that, since the primary circulation is much faster compared to the secondary circulation, the dynamics only 'feel' the averaged perturbation in (canonical) time $\tau$. This is known as 'averaging' and is a generic phenomenon in dynamical

https://doi.org/10.1017/jfm.2017.680 Published online by Cambridge University Press

systems leading to the formation of invariant manifolds (here tori) (Arnol'd 1989). This averaging effect is independent of the particular nature of the perturbations (provided they are weak), thus explaining the observations in Contreras *et al.* (2016*b*) that (weak) fluid inertia as well as convective heat transfer may trigger this behaviour.

(iii) *'Large' Gr*. Here perturbations exceed $O(\epsilon)$ and the Hamiltonian becomes dependent on canonical time $\tau$, i.e. $\mathcal{H} = \mathcal{H}(\zeta_1, \zeta_2, \tau)$, rendering system (3.7) non-autonomous and, generically, non-integrable (Ott 2002). This has fundamental consequences for the flow topology in that some tori disintegrate and (locally) give way to chaotic dynamics while other tori survive and constitute transport barriers. Tori associated with rational streamlines (i.e. emerging as periodic points $\boldsymbol{\Phi}^p(\boldsymbol{x}_k) = \boldsymbol{x}_k$ in the Poincaré section for some finite periodicity $p$) disintegrate into the characteristic island chains surrounded by chaotic regions; tori associated with irrational streamlines (i.e. describing complete concentric curves in said Poincaré section) survive and thus form transport barriers. The fate of the rational and irrational tori in 2D Hamiltonian systems is respectively described by the well-known Poincaré–Birkhoff and KAM theorems (Ott 2002); counterparts of these 'classical' theorems for the current 3D steady flows are given in, for example, Cheng & Sun (1990*a*,*b*). The surviving tori are commonly denoted 'KAM tori' in literature.

The generic response scenario of the flow topology to increasing $Gr$ is demonstrated by the Poincaré section for the previous example $Pr = 0.71$ in figure 4 (only upper-left quadrant $(y, z) \in [0, 1/2] \times [1/2, 1]$ is shown owing to symmetry within plane $x = 1/2$). Case $Gr = 3.2 \times 10^3$ corresponds with the regime of 'small' $Gr$ characterised by the islands within the Poincaré section shown in figure 4(*a*). Note that 'small' and 'large' $Gr$ are distinguished by the corresponding typical perturbation strength and not by the value of $Gr$ itself; the correlation in general is case-specific (here the observed dynamics, for example, imply that $Gr = 3.2 \times 10^3$ yields a perturbation of $O(\epsilon)$). Increasing $Gr$ triggers the response scenarios of the islands (and tori in 3D) associated with 'large' $Gr$. Figure 4(*b*) reveals the emergence of an eleven-island chain at $Gr = 2.4 \times 10^4$ due to the breakdown of a rational torus surrounded by surviving islands (corresponding with KAM tori in 3D). Further increasing $Gr$ progressively triggers further torus breakdown, giving rise to the 'classical' Hamiltonian picture of KAM tori coexisting with island chains accompanied by (ever wider) chaotic bands, as demonstrated in figure 4(*c*) for $Gr = 7.2 \times 10^4$.

The single-wall lid-driven flow (qualitatively) follows the same scenario upon perturbation by, for example, fluid inertia or asymmetric wall forcing (Shankar 1998; Speetjens *et al.* 2006; Ishii, Ota & Adachi 2012; Speetjens & Clercx 2013; Wu *et al.* 2014). This further substantiates their intimate dynamic similarity with the current buoyancy-driven flow and, as a consequence, the universality of the Lagrangian dynamics in 3D steady bounded flows. However, the current flow class admits a more elaborate interplay between fluid-dynamical forces due to, besides viscous and inertial forces, the presence of a third force: buoyancy. This may result in greater dynamic richness (as demonstrated and investigated in § 4).

## 4. Inertia-dominated flow versus thermo-inertial flows

The above demonstrates that the Lagrangian dynamics and generic composition of the flow topology are inextricably linked to (breakdown of) symmetries. The mathematical structure of model (2.3) implies that fluid inertia and convective heat

https://doi.org/10.1017/jfm.2017.680 Published online by Cambridge University Press

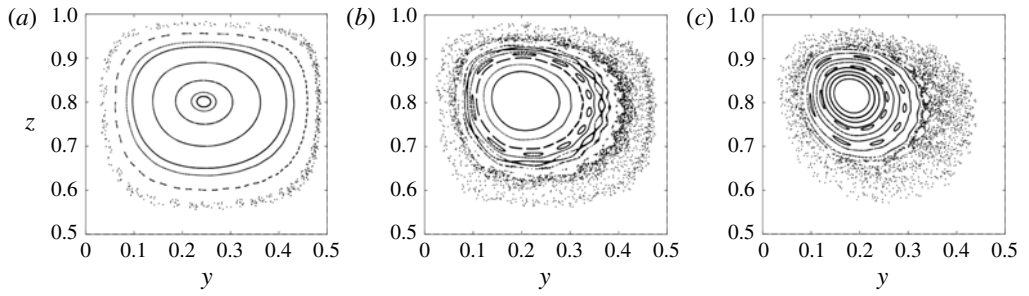



FIGURE 4. Hamiltonian breakdown of toroidal structures with increasing departure from the limit $Gr = 0$ demonstrated for $Pr = 0.71$: (*a*) $Gr = 3.2 \times 10^3$; (*b*) $Gr = 2.4 \times 10^4$; (*c*) $Gr = 7.2 \times 10^4$. Visualisation by intersections with the plane $x = 1/2$ ('Poincaré section'); only upper-left quadrant $(y, z) \in [0, 1/2] \times [1/2, 1]$ is shown owing to symmetry within plane $x = 1/2$.

transfer (via non-zero $Gr$) introduce nonlinearity and thus cause symmetry breaking. Generically this involves (an interplay of) both mechanisms due to the two-way coupling of momentum and energy equations through convective heat transfer and buoyancy. However, the computational studies in Contreras *et al.* (2016*b*) revealed that fluid inertia and convective heat transfer can also independently induce this effect. Furthermore, flow topologies thus formed may under certain conditions undergo bifurcations into more complicated patterns (see, for example, Mallinson & de Vahl Davis 1977; Hiller *et al.* 1989; Yarin *et al.* 1996; Henry & BenHadid 2007). Such observations suggest a non-trivial role and interplay of fluid inertia and convective heat transfer that, to the best of our knowledge, has not been examined in-depth before. The study below seeks to deepen insight into this matter by revisiting the analysis in § 3.4 on the (qualitative) response of the Lagrangian dynamics to increasing the Grashof number from the limit $Gr = 0$. This hinges strongly on the notion that the global 3D flow topology is intimately related to the nature of the stagnation point $\boldsymbol{x}_c = (1/2,\ 1/2,\ 1/2)$. Moreover, this distinguishes between inertia-dominated and thermo-inertial flows (i.e. driven by an interplay of fluid inertia and buoyancy).

### 4.1. *First 'stage' of symmetry breaking: inertia-dominated dynamics*

The nature of the stagnation point $\boldsymbol{x}_c = (1/2,\ 1/2,\ 1/2)$ is determined by the spectral properties of the strain-rate tensor $\boldsymbol{F} = \partial \boldsymbol{u}/\partial \boldsymbol{x}|_{\boldsymbol{x}_c}$ (Guckenheimer & Holmes 1983; Chong, Perry & Cantwell 1990). Symmetries (3.1) and (3.2) imply $\partial u_x/\partial y = \partial u_z/\partial y = 0$ and $\partial u_y/\partial x = \partial u_y/\partial z = 0$, respectively, and in conjunction with incompressibility simplify $\boldsymbol{F}$ to

$$\boldsymbol{F} = \left.\frac{\partial \boldsymbol{u}}{\partial \boldsymbol{x}}\right|_{\boldsymbol{x}_c} = \begin{bmatrix} \partial u_x/\partial x & 0 & \partial u_x/\partial z \\ 0 & -A & 0 \\ \partial u_z/\partial x & 0 & \partial u_z/\partial z, \end{bmatrix}, \quad A = \frac{\partial u_x}{\partial x} + \frac{\partial u_z}{\partial z}, \tag{4.1a,b}$$

in $\boldsymbol{x}_c$. This yields

$$\lambda_1 = -A, \quad \lambda_{2,3} = \frac{A}{2} \pm \sqrt{B}, \quad B = \frac{1}{4}\left[\frac{\partial u_x}{\partial x} - \frac{\partial u_z}{\partial z}\right]^2 + \frac{\partial u_x}{\partial z}\frac{\partial u_z}{\partial x}, \tag{4.2a–c}$$

https://doi.org/10.1017/jfm.2017.680 Published online by Cambridge University Press

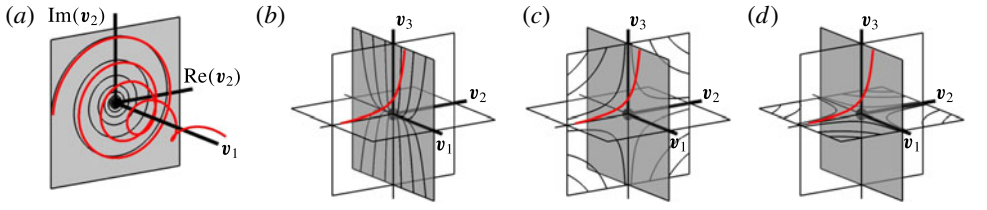



FIGURE 5. (Colour online) Flow topology near stagnation point $\boldsymbol{x}_c$ (black marker) in canonical space spanned by eigenvectors ($\boldsymbol{v}_1$, $\boldsymbol{v}_2$, $\boldsymbol{v}_3$) including typical streamline (red): (*a*) focus with $W_{1D}$ (heavy line) and $W_{2D}$ (shaded); (*b–d*) NSS with here $W_{2D}$ and $W_{1D}$ corresponding with ($\boldsymbol{v}_1$, $\boldsymbol{v}_3$)-plane (shaded) and $\boldsymbol{v}_2$-axis, respectively; (*b*) shows node-type streamline portrait in $W_{2D}$; (*c*,*d*) show saddle-type streamline portraits in transverse ($\boldsymbol{v}_2$, $\boldsymbol{v}_3$)/($\boldsymbol{v}_1$, $\boldsymbol{v}_2$)-planes.

as eigenvalue spectrum, which depends entirely on the planar velocity ($u_x$, $u_z$) in the symmetry plane $\mathcal{P}$. Moreover, it can be shown that the corresponding eigenvectors are of the form $\boldsymbol{v}_1 = \boldsymbol{e}_y$ and $\boldsymbol{v}_{2,3} = \alpha\boldsymbol{e}_x \pm \beta\boldsymbol{e}_z$, signifying orientations normal and parallel, respectively, to said plane. The type of the stagnation point $\boldsymbol{x}_c$ is governed by sign($B$) and, adopting the nomenclature by Chong *et al.* (1990), for incompressible flows ($\boldsymbol{\nabla}\cdot\boldsymbol{u} = \lambda_1 + \lambda_2 + \lambda_3 = 0$) admits two cases: (i) focus for $B < 0$ (complex conjugate eigenvalues $\lambda_{2,3}$); (ii) node/saddle/saddle (NSS) for $B > 0$ (real eigenvalues $\lambda_{2,3}$).

Figure 5(*a*) gives the flow topology near $\boldsymbol{x}_c$ (black marker) in case $\boldsymbol{x}_c$ being a focus including a typical streamline (red). Eigenvector $\boldsymbol{v}_1$ locally defines the corresponding 1D manifold $W_{1D}$ (heavy line) and normal of the 2D manifold $W_{2D}$ (shaded). Orientation $\boldsymbol{v}_1 \in \mathcal{L}$ through the global symmetries according to § 3.2 then readily yields $W_{1D} = \mathcal{L}$ and $W_{2D} = \mathcal{P}$ for a focus-type $\boldsymbol{x}_c$. The eigenvalue spectrum of a NSS-type $\boldsymbol{x}_c$ always comprises a pair of eigenvalues of equal sign and an isolated eigenvalue of opposite sign; the eigenvectors of former and latter locally define $W_{2D}$ and $W_{1D}$, respectively. The streamline portrait within $W_{2D}$ corresponds with a node; the portrait in the two transverse canonical planes corresponds with a saddle. Figure 5(*b–d*) demonstrates this for the case $\mathrm{sign}(\lambda_1) = \mathrm{sign}(\lambda_3) = -\mathrm{sign}(\lambda_2)$, where $W_{2D}$ and $W_{1D}$ correspond with ($\boldsymbol{v}_1$, $\boldsymbol{v}_3$)-plane (shaded) and $\boldsymbol{v}_2$-axis, respectively, and red indicates a typical streamline. The streamline portraits within $W_{2D}$ (*a*) and the transverse ($\boldsymbol{v}_2$, $\boldsymbol{v}_3$)-plane (*b*,*c*) and ($\boldsymbol{v}_1$, $\boldsymbol{v}_2$)-plane (*d*) are shown separately for legibility. Note that figure 5(*b–d*) gives the sole manifold orientation possible for NSS-type $\boldsymbol{x}_c$. This is discussed in § 4.2.

The fact that $\boldsymbol{x}_c$ can either be a focus or NSS implies the following dynamics for the *Gr*-regimes identified in § 3.4.

(i) *Limit* $Gr = 0$. Here symmetry (3.2) 'splits' into symmetries (3.3) and (3.4), yielding $\partial u_x/\partial x = \partial u_z/\partial z = 0$ and thus further simplifying (4.2) to

$$\lambda_1 = 0, \quad \lambda_{2,3} = \pm\sqrt{B_0}, \quad B_0 = \frac{\partial u_x}{\partial z}\frac{\partial u_z}{\partial x}, \tag{4.3a–c}$$

where vanishing of $\lambda_1$ and orientation of its eigenvector as $\boldsymbol{v}_1 = \boldsymbol{e}_y$ reflect the fact that the stagnation point belongs to a stagnation line parallel to the $y$-axis. Differential heating causes fluid to descend and rise at the cold ($x = 0$) and warm ($x = 1$) walls, respectively, inducing weak counter-clockwise rotation about $\boldsymbol{x}_c$ as

https://doi.org/10.1017/jfm.2017.680 Published online by Cambridge University Press

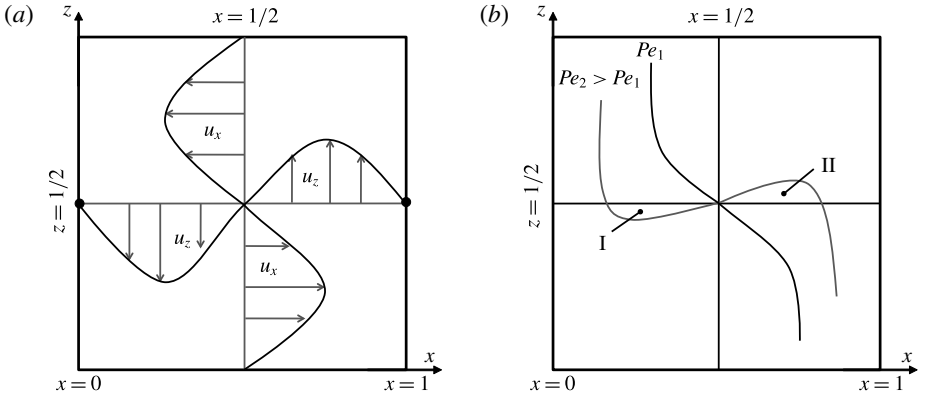



FIGURE 6. Thermal and flow phenomena underlying fundamental Lagrangian dynamics: (*a*) thermally induced counter-clockwise circulation about stagnation point $\boldsymbol{x}_c = (x, z) = (1/2, 1/2)$ due to descent ($u_z < 0$) and ascent ($u_z > 0$) of fluid at the cold ($x = 0$) and warm ($x = 1$) walls, respectively; (*b*) flow-induced penetration of warm and cold temperature fronts in 'cold' ($x < 1/2$) and 'warm' regions ($x > 1/2$), respectively. The latter is illustrated with isotherm $T = 1/2$ for 'weaker' ($Pe_1$) and 'stronger' ($Pe_2 > Pe_1$) convective heat transfer (parameterised by Péclet number $Pe = GrPr$). For 'sufficient' $Pe$ (here $Pe = Pe_2$) this creates local heating (I) and cooling (II) zones adjacent to $\boldsymbol{x}_c$.

shown schematically in figure 6(*a*). This gives rise to $\partial u_x/\partial z < 0$ and $\partial u_z/\partial x > 0$ and, inherently, $B_0 < 0$, implying that $\boldsymbol{x}_c$ is a degenerate focus ($A = 0$), or equivalently, a centre. This is entirely consistent with the observations that $Gr = 0$ yields a primary circulation consisting of concentric streamlines centred on one central stagnation line (see § 3).

(ii) *'Small' Gr*. This induces weak symmetry breaking, i.e. $\partial u_x/\partial x \sim O(\epsilon)$ and $\partial u_z/\partial z \sim O(\epsilon)$, upon substitution in (4.2) yielding $B = B_0 + O(\epsilon^2) \approx B_0 < 0$. Combined with $A = \partial u_x/\partial x + \partial u_z/\partial z \sim O(\epsilon)$ this signifies the transition of the stagnation line into a focus-type stagnation point $\boldsymbol{x}_c$ with manifolds $W_{1D} = \mathcal{L}$ and $W_{2D} = \mathcal{P}$ (figure 5*a*). Hence, the overall vortical structure associated with the primary circulation is preserved. The principal difference with the above limit $Gr = 0$ exists in the formation of toroidal structures on both sides of $\mathcal{P}$ by the Hamiltonian mechanisms discussed in § 3.4.

The above demonstrates that progressively increasing $Gr$ from limit $Gr = 0$ invariably induces a single focus-type stagnation point and, in consequence, a global circulation yielding a flow topology consisting of toroidal structures as illustrated above, advancing this as the universal 'start-up' scenario from said limit. Moreover, the topological equivalence with lid-driven flows established in § 3.3 puts forth fluid inertia as the dominant cause for symmetry breaking. This can be further substantiated by a leading-order approximation of the symmetry-breaking convective and buoyancy terms in (2.3) via decomposition of the flow and temperature fields as $\boldsymbol{u} = \boldsymbol{u}_0 + \boldsymbol{u}'$ and $\widehat{T} = \widehat{T}_0 + \widehat{T}'$, where subscript '0' and primes indicate the symmetric field for limit $Gr = 0$ and associated small non-symmetric departure for 'small' $Gr > 0$, respectively. (Here $\widehat{T}$ corresponds with the redefined temperature according to § 3.2.) This gives

$$-\boldsymbol{\nabla}\widehat{p} + \nabla^2\boldsymbol{u} \approx Gr\boldsymbol{u}_0 \cdot \boldsymbol{\nabla}\boldsymbol{u}_0 - \widehat{T}_0\boldsymbol{e}_z, \quad \nabla^2\widehat{T} = \nabla^2\widehat{T}' \approx GrPr\boldsymbol{u}_0 \cdot \boldsymbol{\nabla}\widehat{T}_0, \qquad (4.4a,b)$$

https://doi.org/10.1017/jfm.2017.680 Published online by Cambridge University Press

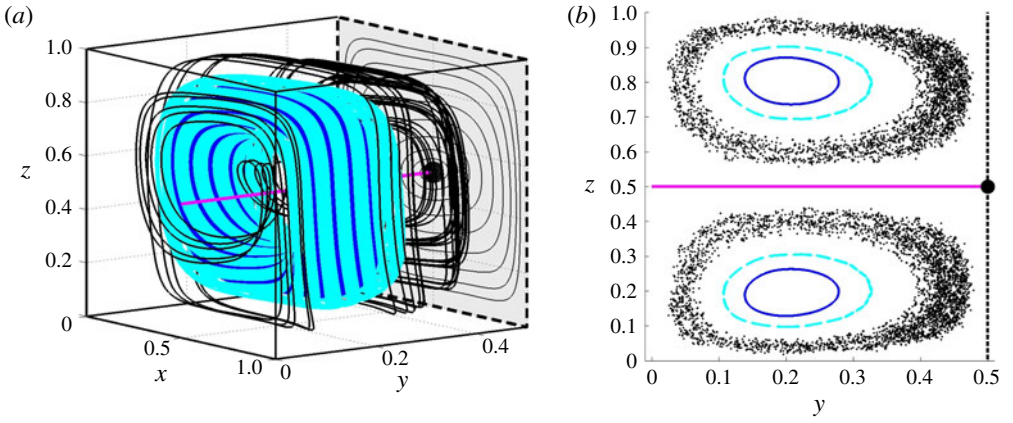



FIGURE 7. (Colour online) Generic 3D flow topology in subregion $0 \leqslant y \leqslant 1/2$ separated by $\mathcal{P}$ (dashed/shaded) in the inertia-dominated regime demonstrated for $Pr = 0.71$ and $Gr = 2.4 \times 10^4$: (*a*) 3D perspective view; (*b*) Poincaré section ($x = 1/2$). Key entities: focus $\boldsymbol{x}_c = (1/2, 1/2, 1/2)$ (black marker) with $\mathcal{P}$ and $\mathcal{L}$ (magenta) as associated 2D manifold and 1D manifold, respectively; KAM torus (blue); torus corresponding with island chains (cyan); 3D chaotic streamline (black).

revealing that the buoyancy term (to leading-order approximation) retains the symmetric form of limit $Gr = 0$ on grounds of its linearity and, indeed, fluid inertia is the prevailing symmetry-breaking mechanism for the flow field in this first stage of $Gr > 0$. Convective heat transfer breaks the symmetry of the temperature field, yet here without appreciable 'feedback' into the momentum balance. This exposes the degree of asymmetry of the buoyancy term, determined by departure $\widehat{T}'$, yet not its presence and/or magnitude per se as cause behind thermally induced non-trivial Lagrangian dynamics. However, this asymmetry becomes significant only for 'sufficiently large' $Gr$, as investigated in § 4.2.

Figure 7(*a*) exemplifies the generic 3D flow topology in the inertia-dominated regime with case $Pr = 0.71$ and $Gr = 2.4 \times 10^4$. (The inertia-dominated case corresponds with the state denoted in the literature by, for example, 'single-roll base flow', 'one-roll system' or 'one-roll convective cell' (Mallinson & de Vahl Davis 1977; Hiller *et al.* 1989; Yarin *et al.* 1996)) The key organising entities are the focus $\boldsymbol{x}_c$ (black marker), with $\mathcal{P}$ (dashed/shaded) and $\mathcal{L}$ (magenta) as associated 2D manifold $W_{2D}(\boldsymbol{x}_c)$ and 1D manifold $W_{1D}(\boldsymbol{x}_c)$, respectively. The flow topology in each subregion separated by $\mathcal{P}$ consists of a single family of KAM tori (one specimen highlighted in blue) and island chains emanating from disintegrated tori (one specimen highlighted in cyan) centred on $W_{1D}(\boldsymbol{x}_c)$. These structures are typically surrounded by chaotic streamlines (one specimen indicated in black). Figure 7(*b*) gives the corresponding Poincaré section (plane $x = 1/2$) of this generic topological composition. (The 3D view includes only a small part of the chaotic streamline for reasons of legibility.) Centrifugal forces cause outward spiralling away from $\boldsymbol{x}_c$ within $\mathcal{P}$, implying repulsion in $W_{2D}(\boldsymbol{x}_c)$ (i.e. $Re(\lambda_{2,3}) = A/2 > 0$) and, in consequence, attraction along $W_{1D}(\boldsymbol{x}_c)$ (i.e. $\lambda_1 = -A = -2Re(\lambda_{2,3}) < 0$). This renders the 1D and 2D manifolds stable ($W^s_{1D}$) and unstable ($W^u_{2D}$), respectively, in dynamical-systems terminology (Guckenheimer & Holmes 1983; Ott 2002). The attraction along $W^s_{1D}$ drives the secondary circulation.

https://doi.org/10.1017/jfm.2017.680 Published online by Cambridge University Press

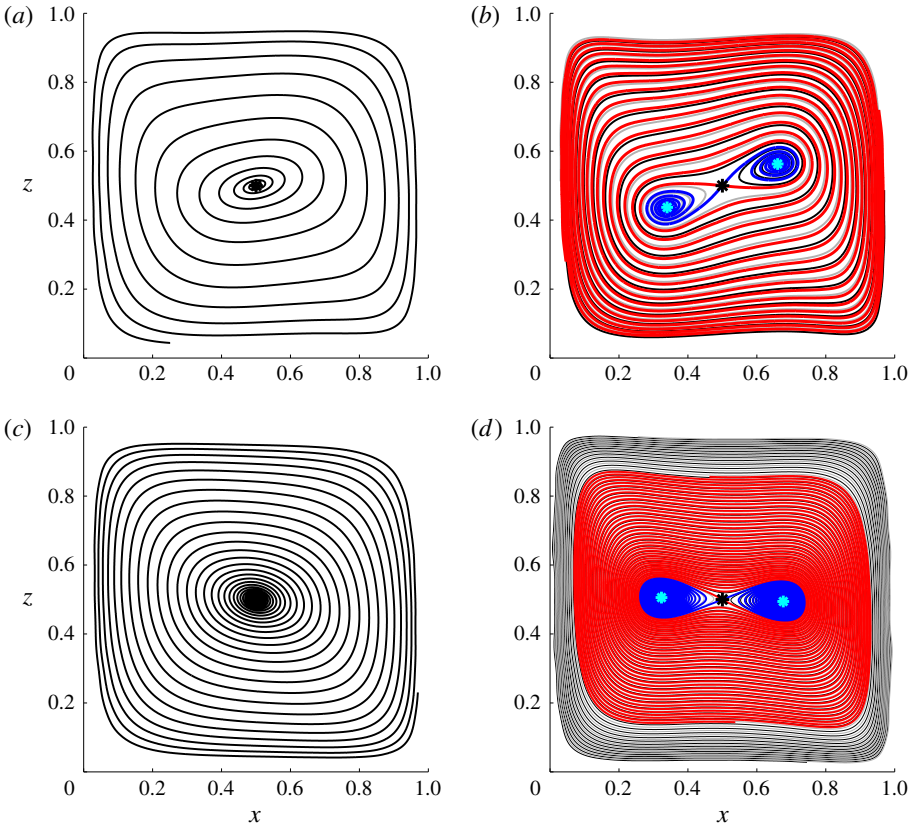



FIGURE 8. (Colour online) Typical streamline portraits in $\mathcal{P}$ before (*a*,*c*) and after (*b*,*d*) bifurcation of the central stagnation point (black marker) from focus to saddle (NSS in 3D) with accompanying pair of foci (cyan markers) demonstrated for $Pr = 0.71$ (*a*,*b*) and $Pr = 7$ (*c*,*d*): (*a*) pre-bifurcation ($Gr = 2.4 \times 10^4$); (*b*) post-bifurcation ($Gr = 7.2 \times 10^4$); (*c*) pre-bifurcation ($Gr = 1.3 \times 10^3$); (*d*) post-bifurcation ($Gr = 1.0 \times 10^4$). Blue streamline: stable manifold of saddle forming heteroclinic orbits with foci; red streamline: unstable manifold of saddle separating 2D manifolds of foci within the symmetry plane; black/grey curves: typical streamlines within each 2D manifold.

### 4.2. *Second 'stage' of symmetry breaking: thermo-inertial flows*

Convective heat transfer becomes stronger with increasing $Gr$ and thus, for 'sufficient' $Gr$, causes symmetry breaking of the temperature field and, in consequence, of the buoyancy term to such an extent that it induces a global bifurcation in the flow topology, as demonstrated in figure 8 for the streamline portrait in $\mathcal{P}$ for $Pr = 0.71$ (top) and $Pr = 7$ (bottom). The stagnation point $\boldsymbol{x}_c$ (black marker) within $\mathcal{P}$ bifurcates from a focus for 'smaller' $Gr$ (panel *a*,*c*) to a saddle for 'larger' $Gr$ (panel *b*,*d*). Moreover, saddle-type $\boldsymbol{x}_c$ is accompanied by a pair of foci (cyan markers) arranged symmetrically according to centro-symmetry (3.2). The stable manifold of the saddle (blue streamline) forms heteroclinic orbits with the repelling foci; its unstable manifold (red streamline) separates the 2D manifolds of the foci within the symmetry plane (as demonstrated by typical streamlines in each 2D manifold indicated by the black/grey curves). This heteroclinic interaction gives rise to the 'figure 8' pattern emerging around $\boldsymbol{x}_c$.

https://doi.org/10.1017/jfm.2017.680 Published online by Cambridge University Press

The general sense of circulation is retained upon bifurcation: fluid revolves in counter-clockwise direction around the pre-bifurcation focus as well as about the post-bifurcation individual foci (blue streamline) and the entire saddle–node arrangement (red streamline). Note that the bifurcated state is termed 'two-roll system' in Hiller *et al.* (1989), Yarin *et al.* (1996); the vortical structures centred on the foci (blue) are denoted 'secondary rolls' in Mallinson & de Vahl Davis (1977).

The above behaviour corresponds with a pitchfork bifurcation of the streamline pattern within $\mathcal{P}$ at stagnation point $\boldsymbol{x}_c$ (Ott 2002). This is a direct consequence of two fundamental topological properties. First, centro-symmetry (3.2) causes stagnation points in the midplane other than $\boldsymbol{x}_c$ to emerge pair-wise following $(\boldsymbol{x}_s, \boldsymbol{S}_{ii}(\boldsymbol{x}_s))$. Second, the Poincaré-Hopf theorem states that the sum of the Poincaré indices $I_i$ of fixed (here stagnation) points equals the Euler characteristic $\chi$ of the invariant surface, i.e.

$$\chi = \sum_{i=1}^{N} I_i, \tag{4.5}$$

where $I = 1$ and $I = -1$ for focus-type and saddle-type stagnation points, respectively (Henle 1979). The Euler characteristic is a topological invariant for the invariant material plane $\mathcal{P}$ and, given 'small' $Gr$ always results in a single focus, here equals $\chi = 1$. Preservation of $\chi = 1$ during bifurcation of $\boldsymbol{x}_c$ within $\mathcal{P}$ from focus to saddle thus dictates the emergence of a symmetric pair of focus-type stagnation points. (This again ignores the above-mentioned corner eddies and thus, strictly, pertains only to the subregion within $\mathcal{P}$ that excludes the corner regions. Moreover, this assumes that the separatrix between former and latter regions is unaffected by the bifurcation. However, given their localised and weak nature, the corner eddies changing due to the bifurcation and thereby simultaneously compromising the separatrix – and thus the reasoning in toto – is highly improbable.) The stagnation points in $\mathcal{P}$ may possibly undergo subsequent bifurcations upon further increasing $Gr$. However, this is beyond the present scope.

The above focus-to-saddle transition corresponds in the 3D domain with a bifurcation of $\boldsymbol{x}_c$ from focus to NSS. The fact that topological constraints only admit saddle-type streamline portraits for $\boldsymbol{x}_c$ within $\mathcal{P}$ upon bifurcation has the fundamental implication that manifold $W_{2D}$ (accommodating node-type portraits) can not coincide with $\mathcal{P}$ and here, given $\boldsymbol{v}_1 \in \mathcal{L}$ and $\boldsymbol{v}_{2,3} \in \mathcal{P}$, thus must emerge from either the $(\boldsymbol{v}_1, \boldsymbol{v}_2)$-plane or the $(\boldsymbol{v}_1, \boldsymbol{v}_3)$-plane. Hence, strictly two configurations are permissible:

(i) $\mathrm{sign}(\lambda_1) = \mathrm{sign}(\lambda_3) = -\mathrm{sign}(\lambda_2) \Rightarrow (\boldsymbol{v}_1, \boldsymbol{v}_3) \rightarrow W_{2D}, \boldsymbol{v}_2 \rightarrow W_{1D}$;
(ii) $\mathrm{sign}(\lambda_1) = \mathrm{sign}(\lambda_2) = -\mathrm{sign}(\lambda_3) \Rightarrow (\boldsymbol{v}_1, \boldsymbol{v}_2) \rightarrow W_{2D}, \boldsymbol{v}_3 \rightarrow W_{1D}$.

However, given that $\lambda_{2,3}$ and associated eigenvectors $\boldsymbol{v}_{2,3} \in \mathcal{P}$ can be interchanged without loss of generality, both cases are in fact identical. Thus the former case, shown in figure 5(*b–d*), defines the generic configuration for NSS-type $\boldsymbol{x}_c$, putting forth $W_{1D} \in \mathcal{P}$ and (near $\mathcal{P}$) $W_{2D} \perp \mathcal{P}$ as corresponding 3D manifold orientations (typical configurations are demonstrated in § 5.2.1). Moreover, $\mathrm{sign}(\lambda_2) = -\mathrm{sign}(\lambda_3)$ via (4.2) gives inequality $\lambda_2\lambda_3 = A^2/4 - B \leqslant 0$. Hence, $B = 0$ implies $A = 0$, meaning that the pitchfork bifurcation always happens through the degenerate case $\lambda_1 = \lambda_2 = \lambda_3 = 0$.

Figure 9(*a*) gives the Poincaré section ($x = 1/2$) corresponding with $(Pr, Gr) = (7, 1.0 \times 10^4)$ as shown in figure 8(*d*), exposing a secondary family of KAM tori around the symmetry line $\mathcal{L}$ at the cavity wall $y = 0$, accommodating secondary

https://doi.org/10.1017/jfm.2017.680 Published online by Cambridge University Press

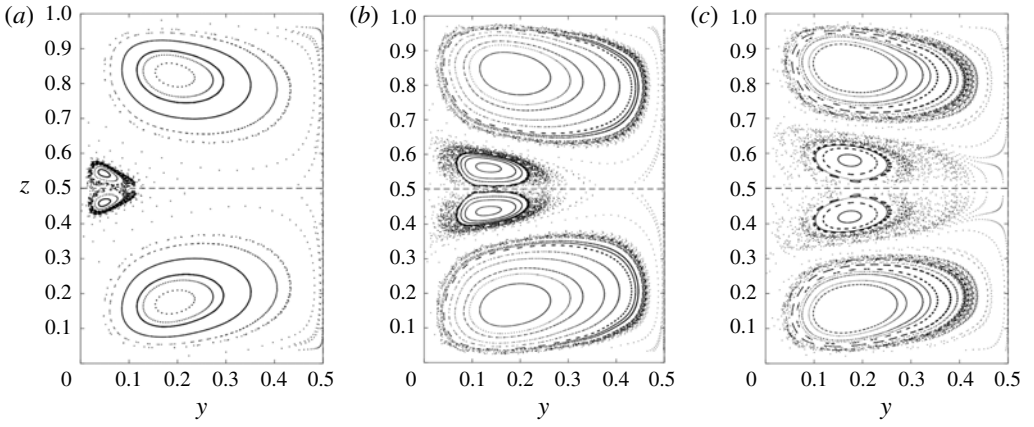



FIGURE 9. Emergence of secondary family of KAM tori around $\mathcal{L}$ (dashed) at cavity wall $y = 0$ and its expansion with growing $Gr$ demonstrated for $Pr = 7$: (*a*) $Gr = 1.0 \times 10^4$; (*b*) $Gr = 1.7 \times 10^4$; (*c*) $Gr = 2.5 \times 10^4$. Visualisation by the left half ($0 \leqslant y \leqslant 1/2$) of Poincaré sections ($x = 1/2$).

circulation in the reversed direction of the original ('primary') family of tori (i.e. counter-clockwise and clockwise secondary circulation for primary and secondary tori, respectively). Such secondary tori have, to the best of our knowledge, not been explicitly reported before. (The two tori families are reminiscent of the two kinds of spiralling streamlines, distinguished by 'forward' and 'reversed' flow, in the post-bifurcation case in Mallinson & de Vahl Davis (1977). However, the fact that the latter (i) include (one of) the secondary roll(s) and (ii) involve secondary circulation in directions opposite to that of the above tori strongly suggests that these are essentially different entities. The 'forward-flow' streamlines adjacent to the $y$-wise endwalls likely result from the $y$-wise elongated cavity (height : width $= 1:2$) and therefore have no counterpart in the current cubic cavity. Moreover, comparison with findings in § 5.2 suggests that the 'reversed-flow' streamlines adjacent to symmetry plane $\mathcal{P}$ belong to the chaotic region in between primary and secondary tori.) The spatial extent of these new entities expands (while maintaining circulation direction) with increasing $Gr$, as demonstrated in figure 9(*b*,*c*) for $Gr = 1.7 \times 10^4$ and $Gr = 2.5 \times 10^4$, respectively, at $Pr = 7$. Moreover, their emergence is a consequence of intricate 3D heteroclinic interactions between the manifolds of the above-mentioned stagnation points in $\mathcal{P}$ and new stagnation points on $\mathcal{L}$. This is further studied in § 5.

The pitchfork bifurcation has been observed in numerous studies in both 2D and 3D systems, see, for example, de Vahl Davis (1968), Mallinson & de Vahl Davis (1973), Mallinson & de Vahl Davis (1977), de Vahl Davis (1983), Markatos & Pericleous (1984), Hiller *et al.* (1989), Hiller *et al.* (1990), Yarin *et al.* (1996), and occurs in a similar way for basically any $Pr$. The impact of the latter is mainly quantitative in that secondary circulation becomes weaker with increasing $Pr$, and streamlines, in consequence, tend towards denser winding; compare to this end, for example, figure 8(*b*,*d*) and refer, for example, also to Mallinson & de Vahl Davis (1977).

### 4.3. *Bifurcation mechanism*

The pitchfork bifurcation for 'sufficiently large' $Gr$ admits physical explanation by continuing the examination of the properties of the stagnation point $\boldsymbol{x}_c$ in § 4.1.

https://doi.org/10.1017/jfm.2017.680 Published online by Cambridge University Press

Transition of $\boldsymbol{x}_c$ from a focus into a NSS happens for parameter $B \geqslant 0$ in (4.2) and thus advances

$$B \geqslant 0 \quad \Rightarrow \quad B_0 \geqslant B_0^* \quad \text{with } B_0^* = -\frac{1}{4}\left[\frac{\partial u_x}{\partial x} - \frac{\partial u_z}{\partial z}\right]^2 < 0, \tag{4.6}$$

as the kinematic bifurcation criterion. For (generically) non-zero $\partial u_{x,z}/\partial x, z$ this sets a negative lower bound for $B_0$ (as opposed to $B_0 \geqslant 0$ above), meaning that the flow admits the bifurcation for a circulation in the sense shown in figure 6(*a*). Hence, this is indeed the first (in a possible sequence of) bifurcation(s) undergone by the streamline pattern set up at $Gr = 0$. Physical considerations suggest that stronger convective heat transfer (by increasing Péclet number $Pe = GrPr$ through, for given $Pr$, increasing $Gr$) promotes exceeding threshold (4.6) and, inherently, the bifurcation. Stronger convective heat transfer namely admits deeper penetration of the warm and cold temperature fronts in the 'cold' ($x < 1/2$) and 'warm' regions ($x > 1/2$), respectively, in a manner as illustrated in figure 6(*b*) with isotherm $T = 1/2$. (Symmetry dictates this isotherm to remain attached to the stagnation point $\boldsymbol{x}_c$ and satisfy centro-symmetry (3.2) for any $Gr$ and $Pr$.) The latter (and any other isotherm) emanates from 'coiling up' of the vertical isotherms of limit $Gr = 0$ shown in figure 2(*a*) due to the circulation about the cavity centre for $Gr > 0$. The convolution becomes more pronounced with increasing $Pe = GrPr$, and thus causes ever deeper penetration of said temperature fronts. For $Pe = GrPr$ beyond a certain threshold ($Pe_2$ in figure 6*b*) this results in formation of local heating (I) and cooling (II) zones adjacent to $\boldsymbol{x}_c$. This locally reduces buoyancy and, in consequence, flattens the $u_z$-profile (and, via continuity, also the $u_x$-profile), thus effectively shifting $B_0 < B_0^* < 0$ towards threshold $B_0 = B_0^*$ following (4.6). The bifurcation occurs when the shift suffices to cross this threshold, or equivalently, an associated threshold $Gr^*$.

The pitchfork bifurcation happens at any $Pr$ upon exceeding $Gr = Gr^*$, as confirmed by the corresponding bifurcation diagram in figure 10. Moreover, this reveals, consistent with figure 8, a decreasing threshold $Gr^*$, and thus earlier bifurcation, with growing $Pr$. This stems from the existence of two limits of the governing equations (2.3) in $Pr$. Limit $Pr = 0$: symmetry breaking solely by fluid inertia due to the absence of convective heat transfer; limit $Pr \to \infty$: symmetry breaking dominated by buoyancy via strongly asymmetric temperature fields due to purely convective heat transfer. The former and latter imply absence and immediate onset, respectively, of the pitchfork bifurcation on the route starting from limit $Gr = 0$ and define asymptotes for the bifurcation threshold following

$$\lim_{Pr \to 0} Gr^* \to \infty, \qquad \lim_{Pr \to \infty} Gr^* = 0, \tag{4.7a,b}$$

which qualitatively 'shape' the bifurcation diagram. (Temperature becomes a passive tracer for unbounded $Pr$, i.e. $\lim_{Pr\to\infty} \mathrm{d}T/\mathrm{d}t = \boldsymbol{u} \cdot \boldsymbol{\nabla} T = 0$, causing direct transport of temperature fronts with material fluid interfaces via the incipient circulation sketched in figure 6(*a*), and thus their immediate penetration according to figure 6(*b*).) The threshold monotonically decreases with growing $Pr$ during the transition from inertia-dominated ('small' $Pr$) to buoyancy-dominated ('large' $Pr$) symmetry breaking. Asymptotes (4.7) suggest a hyperbolic relation $Gr^* = aPr^b$; the dashed curve in figure 10 gives this relation using coefficients $(a, b) = (2.53 \times 10^4, -0.97)$ determined via the least-squares method.

The above designates buoyancy as the mechanism that underlies the pitchfork bifurcation, and $Gr$ as its key control parameter, and thus rigorously supports

https://doi.org/10.1017/jfm.2017.680 Published online by Cambridge University Press

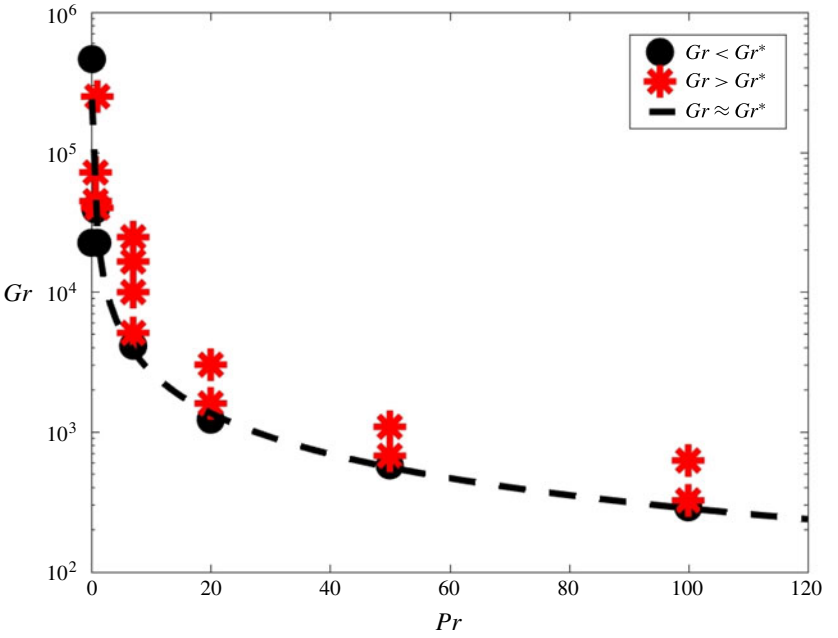



FIGURE 10. (Colour online) Bifurcation diagram for the pitchfork bifurcation: threshold $Gr^*$ versus $Pr$. Symbols indicate data points from numerical simulations; the dashed curve indicates the approximate bifurcation threshold $Gr \approx aPr^b$, with coefficients $(a,b) = (2.53 \times 10^4, -0.97)$.

phenomenological explanations in the literature (as, for example, in de Vahl Davis (1968), Mallinson & de Vahl Davis (1977)). It furthermore substantiates the earlier finding in § 4.1 that, irrespective of $Pr$, the formation of a single global vortical structure as illustrated in figure 7 is the only possible 'start-up' scenario of the flow upon increasing $Gr$ from zero. Hence, the bifurcation into a more complex vortical structure must (for realistic $Pr$) happen at some finite $Gr$, and thus is an essentially nonlinear phenomenon.

The bifurcated streamline pattern is reminiscent of that occurring in lid-driven cavity flows with simultaneous forcing by facing walls moving steadily at the same speed in opposite direction (Kelmanson & Lonsdale 1996; Shankar 1998). This extends the link with lid-driven cavity flows established in § 3. However, important to note is that this second connection exists only for the post-bifurcation case, in other words, for $Gr$ above some finite lower bound. A linear limit $Gr = 0$ topologically equivalent to two-wall lid-driven flows is non-existent.

## 5. Typical 3D flow topologies for thermo-inertial flows

### 5.1. *General behaviour associated with the pitchfork bifurcation*

The streamline patterns corresponding with the cases in the bifurcation diagram, and comparison with the literature (Mallinson & de Vahl Davis 1977; Yarin *et al.* 1996), strongly suggests that, overall, the bifurcated 3D flow topologies are qualitatively similar (at least) up to $Pr \sim O(6 \times 10^3)$. Two fundamentally different situations can be distinguished in this range: cases with and without secondary tori.

https://doi.org/10.1017/jfm.2017.680 Published online by Cambridge University Press

The bifurcated 3D topologies of cases $Pr = 7$ and $Pr = 0.71$ in figure 8, for example, correspond to former and latter situations, respectively. Secondary tori are separated from the primary tori by a 'separatrix' formed by intricate 3D heteroclinic manifold interactions of stagnation points on $\mathcal{P}$ and $\mathcal{L}$ (elaborated in § 5.2) and are for the cases included in the bifurcation diagram found only for $Pr \geqslant 7$; they are absent for all 'smaller' $Pr$ (here $Pr \leqslant 1$). This suggests that secondary tori emerge only for 'larger' $Pr$ due to topological bifurcation(s) within regime $Gr \geqslant Gr^*$ corresponding with the Prandtl number $Pr$. Given the transition from inertia-dominated to buoyancy-dominated dynamics with increasing $Pr$ (§ 4.3), this designates secondary tori as a buoyancy-induced phenomenon that occurs upon exceeding a certain threshold $Pr^*$. (Thus dividing regime $Gr > Gr^*$ in the bifurcation diagram in figure 10 into subregimes $Pr \leqslant Pr^*$ and $Pr > Pr^*$.) Moreover, secondary tori always appear at the cavity endwalls and gradually expand towards $\mathcal{P}$ with increasing $Gr$ in a similar way as demonstrated in figure 9 for $Pr = 7$. Hence, the bifurcated flow topology at $Pr = 7$ is typical of that for 'larger' $Pr$ (i.e. $Pr > Pr^*$) in general. Note for reference that Prandtl numbers of realistic fluids span many orders of magnitude, ranging from $Pr \sim O(10^{-2})$ for liquid metals via $Pr \sim O(1)$ and $Pr \sim O(10)$ for air and water, respectively, to $Pr \sim O(10^4 - 10^8)$ for magma (Lappa 2010).

Furthermore, the saddle-foci arrangement may undergo stability reversal upon further increasing $Gr$: foci become attracting within $\mathcal{P}$ and form a heteroclinic orbit with the unstable manifold of the saddle. Concurrently with stability reversal, a closed streamline emerges within $\mathcal{P}$ that encloses the saddle-foci arrangement and acts as a repelling limit cycle for the stable manifold of the saddle. The flow topology inside the area enclosed by the limit cycle nonetheless remains as in figure 8(*b*,*d*), yet with now the unstable and stable manifold of the saddle coiling up around the foci and spiralling outward, respectively, in counter-clockwise direction (thus maintaining the sense of the primary circulation). Such stability reversal, for example, happens for $Pr = 7$ between $Gr = 1.7 \times 10^4$ (original stability) and $Gr = 2.5 \times 10^4$ (reversed stability). However, the impact on the flow topology is marginal and localised in that certain heteroclinic interactions between the several stagnation points may change yet without essentially affecting the overall structure and role of the above-mentioned separatrix. The global partitioning into two families of KAM tori (and the corresponding sense of circulation) is retained, as evidenced by the (qualitatively) identical composition of the Poincaré sections for $Gr = 1.0 \times 10^4$, $1.7 \times 10^4$ (original stability) and $2.5 \times 10^4$ (reversed stability) in figure 9. Hence, stability reversal, given its secondary role in the global 3D Lagrangian dynamics, is not examined further here.

Typical bifurcated 3D flow topologies with and without secondary tori are demonstrated below in §§ 5.2 and 5.3, respectively. First insights into the mechanisms underlying their 3D structure and organisation are obtained through analysis of heteroclinic interactions between the several stagnation points.

### 5.2. *Presence of secondary tori (fluids with 'larger' Pr)*

#### 5.2.1. *Stagnation points and associated manifolds*

Case $Pr = 7$ and $Gr = 2.5 \times 10^4$ is adopted hereafter as a typical bifurcated 3D flow topology with secondary tori as occurring for 'larger' $Pr$ (i.e. $Pr > Pr^*$). The stagnation points here consist of the above-mentioned NSS ($\boldsymbol{n}_{\mathcal{P}}$) and pair of foci ($\boldsymbol{f}_{\mathcal{P},1}$ and $\boldsymbol{f}_{\mathcal{P},2}$) within $\mathcal{P}$ and a single NSS ($\boldsymbol{n}_{\mathcal{L}}$) and focus ($\boldsymbol{f}_{\mathcal{L}}$) on $\mathcal{L}$.

https://doi.org/10.1017/jfm.2017.680 Published online by Cambridge University Press

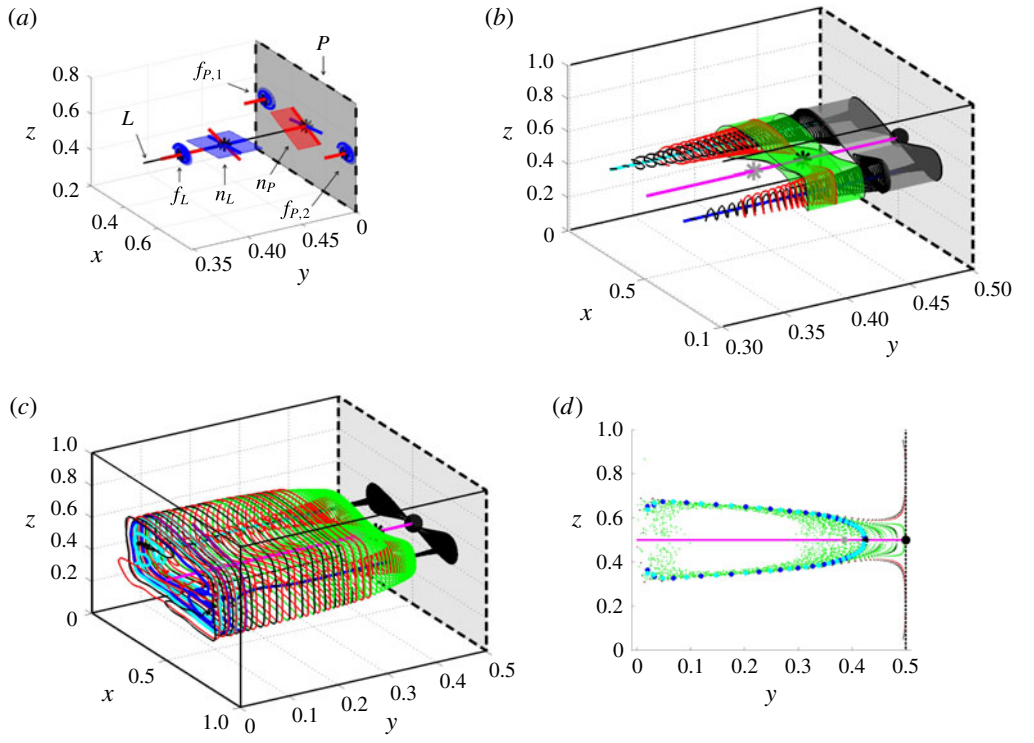



FIGURE 11. (Colour online) Typical configuration of stagnation points in symmetry plane/line ($\mathcal{P}/\mathcal{L}$) and associated manifolds in bifurcated 3D flow topology demonstrated for $Pr = 7$ and $Gr = 2.5 \times 10^4$: (*a*) stagnation points ($\boldsymbol{f}_{\mathcal{P},1,2}$, $\boldsymbol{n}_{\mathcal{P}}$, $\boldsymbol{f}_{\mathcal{L}}$, $\boldsymbol{n}_{\mathcal{L}}$) (black stars) and local orientation of associated 1D (lines) and 2D (planes/disks) manifolds (blue/red: stable/unstable); (*b*) 3D manifold configuration encompassing $W^u_{1D}(\boldsymbol{f}_{\mathcal{P},1,2})$ (blue/cyan), $W^u_{2D}(\boldsymbol{n}_{\mathcal{P}})$ (grey/black), $W^u_{1D}(\boldsymbol{n}_{\mathcal{L}})$ (red), $W^s_{2D}(\boldsymbol{n}_{\mathcal{L}})$ (green) and heteroclinic orbit $\mathcal{L} = (W^u_{2D}(\boldsymbol{n}_{\mathcal{P}}) \cap W^s_{2D}(\boldsymbol{n}_{\mathcal{L}})) \cup W^s_{1D}(\boldsymbol{f}_{\mathcal{L}})$ (magenta); (*c*) global foliation of manifolds ($W_{2D}$ represented by single constituent streamline); (*d*) Poincaré section $x = 1/2$ (shows larger portions of streamlines than in panel *c*). Note that $W^u_{2D}$ of $\boldsymbol{f}_{\mathcal{L}}$ (grey marker in panels *b–d*) is not included due to its localised nature.

(Note that all non-degenerate stagnation points in incompressible flows are either NSS or focus; Chong *et al.* (1990).) Figure 11(*a*) gives the position of the stagnation points (black stars) including the local orientation of the associated 1D/2D manifold pairs (extent exaggerated for visibility) spanned by the corresponding eigenvectors $\boldsymbol{v}$ of the strain-rate tensor $\boldsymbol{F}$. 1D manifolds ($W_{1D}$) are indicated by lines; 2D manifolds ($W_{2D}$) are indicated by planes and disks for NSSs and foci, respectively. Blue/red objects represent stable ($W^s$) and unstable ($W^u$) manifolds; heavy lines and spirals within 2D manifolds indicate principal axes and typical trajectory for NSSs and foci, respectively. Note that the eigenvector(s) spanning a certain 1D/2D manifold are on grounds of symmetry either parallel or normal to $\mathcal{P}$. The specific manifold configurations are ($W^s_{1D}$, $W^u_{2D}$) for $\boldsymbol{n}_{\mathcal{P}}$ (oriented as $W_{1D} \in \mathcal{P}$ and $W_{2D} \perp \mathcal{P}$ following § 4.2) and ($W^u_{1D}$, $W^s_{2D}$) for all other stagnation points.

The general 3D manifold structure and configuration are demonstrated in figure 11(*b*). Manifolds $W^u_{1D}(\boldsymbol{f}_{\mathcal{P},1,2})$ (blue/cyan streamlines) emerge perpendicularly from $\mathcal{P}$ and initially run parallel to $\mathcal{L}$ (magenta). Note that a first schematic of $W^u_{1D}(\boldsymbol{f}_{\mathcal{P},1,2})$ is

https://doi.org/10.1017/jfm.2017.680 Published online by Cambridge University Press

provided in Hiller *et al.* (1989). Line $\mathcal{L}$, in turn, constitutes the heteroclinic orbits between $\boldsymbol{n}_{\mathcal{P}}$ (black sphere), $\boldsymbol{n}_{\mathcal{L}}$ (black star) and $\boldsymbol{f}_{\mathcal{L}}$ (grey star). Manifold $W^u_{2D}(\boldsymbol{n}_{\mathcal{P}})$, part of which is delineated by the grey stream surface bounded by heavy black streamlines, emanates in two directions from $\mathcal{L}$ and subsequently coils up on each side around $W^u_{1D}(\boldsymbol{f}_{\mathcal{P},1})$ and $W^u_{1D}(\boldsymbol{f}_{\mathcal{P},2})$ while gradually 'spiralling away' from $\mathcal{P}$. This underlies the secondary rolls reported in Mallinson & de Vahl Davis (1977). (Here the final segment of the shown part of $W^u_{2D}(\boldsymbol{n}_{\mathcal{P}})$ is visualised only by the bounding streamline starting closest to $\mathcal{P}$.) Manifold $W^s_{2D}(\boldsymbol{f}_{\mathcal{L}})$ (grey star) is highly localised due to rapid disintegration already at small distances from $\mathcal{L}$. Hence, this entity is not included in figure 11 for reasons of legibility and, given its minor role, omitted in the remaining discussion.

Manifold $W^u_{1D}(\boldsymbol{n}_{\mathcal{L}})$ (red streamline) shadows individual streamlines within $W^u_{2D}(\boldsymbol{n}_{\mathcal{P}})$ by coiling up around $W^u_{1D}(\boldsymbol{f}_{\mathcal{P},1,2})$ while spiralling away from $\mathcal{P}$ in essentially the same way. Manifold $W^s_{2D}(\boldsymbol{n}_{\mathcal{L}})$ is partially delineated by the green stream surface (bounded by thin black streamlines) and emanates in two directions from $\mathcal{L}$ in a manner resembling $W^u_{2D}(\boldsymbol{n}_{\mathcal{P}})$. However, an essential difference between both entities is that $W^s_{2D}(\boldsymbol{n}_{\mathcal{L}})$, instead of coiling up individually around $W^u_{1D}(\boldsymbol{f}_{\mathcal{P},1})$ and $W^u_{1D}(\boldsymbol{f}_{\mathcal{P},2})$, layers itself around the entire structure defined by $W^u_{2D}(\boldsymbol{n}_{\mathcal{P}})$ and $W^u_{1D}(\boldsymbol{n}_{\mathcal{L}})$.

Figure 11(*b*) exposes the central role of manifolds $W^u_{1D}$ of foci $\boldsymbol{f}_{\mathcal{P},1,2}$ in the global 3D flow topology by 'arranging' all other manifolds. The latter continue to closely follow manifolds $W^u_{1D}(\boldsymbol{f}_{\mathcal{P},1,2})$ while foliating throughout the entire 3D domain, as demonstrated in figure 11(*c*,*d*), which further substantiates this central role. (Here $W^u_{2D}(\boldsymbol{n}_{\mathcal{P}})$ and $W^s_{2D}(\boldsymbol{n}_{\mathcal{L}})$ are each represented by way of a single constituent streamline.) Moreover, this reveals that manifolds $W^u_{1D}(\boldsymbol{f}_{\mathcal{P},1,2})$ set up a secondary circulation normal to $\mathcal{P}$ akin to the inertia-dominated regime, which is particularly visible in the corresponding Poincaré section in figure 11(*d*). Note that the latter corresponds with larger portions of the streamlines than shown in figure 11(*c*). Comparison of figure 11(*d*) with figure 9(*c*) reveals that manifolds $W^u_{1D}(\boldsymbol{f}_{\mathcal{P},1,2})$ outline the above-mentioned separatrix between the primary and secondary KAM tori. This is elaborated in § 5.2.2.

The Poincaré section of $W^s_{2D}(\boldsymbol{n}_{\mathcal{L}})$ (green markers) clearly signifies chaotic behaviour that, given being interspersed with the Poincaré sections of $W^u_{2D}(\boldsymbol{n}_{\mathcal{P}})$ (black markers), $W^u_{1D}(\boldsymbol{n}_{\mathcal{L}})$ (red markers) and $W^u_{1D}(\boldsymbol{f}_{\mathcal{P},1,2})$ (blue/cyan markers), ensues from heteroclinic intersections $W^s_{2D}(\boldsymbol{n}_{\mathcal{L}}) \cap W^u_{2D}(\boldsymbol{n}_{\mathcal{P}})$ and $W^u_{1D}(\boldsymbol{f}_{\mathcal{P},1,2}) \cap W^s_{2D}(\boldsymbol{n}_{\mathcal{L}})$ and homoclinic intersections $W^s_{2D}(\boldsymbol{n}_{\mathcal{L}}) \cap W^u_{1D}(\boldsymbol{n}_{\mathcal{L}})$. Intersections between these manifolds (and possibly those of further undetected stagnation points) namely are signatures of chaotic dynamics (Ott 2002; Meiss 2015). Note that $W^u_{1D}(\boldsymbol{n}_{\mathcal{L}})$ and $W^u_{2D}(\boldsymbol{n}_{\mathcal{P}})$ cannot intersect on grounds of equal stability properties. Moreover, restriction of $W^s_{1D}(\boldsymbol{n}_{\mathcal{P}})$ to $\mathcal{P}$ due to reflectional symmetry (3.1) excludes this entity from involvement in the 3D chaotic dynamics.

### 5.2.2. *Arrangement of coherent structures*

The 1D manifolds $W^u_{1D}$ of foci $\boldsymbol{f}_{\mathcal{P},1,2}$ tend to converge on NSS $\boldsymbol{n}_{\mathcal{L}}$, which must be attributed to the heteroclinic intersections $W^u_{1D}(\boldsymbol{f}_{\mathcal{P},1,2}) \cap W^s_{2D}(\boldsymbol{n}_{\mathcal{L}})$, and thus describe a cocoon-like 'skeleton' that forms the 'backbone' of a chaotic region. This structure is clearly outlined by the blue/cyan markers and curves in figures 11(*d*) and 12(*a*), respectively, and partitions the subregion on each side of $\mathcal{P}$ into a zone interior and exterior to the skeleton. Thus the skeleton constitutes the above-mentioned separatrix between primary (exterior zone) and secondary (interior zone) tori. The skeleton consisting of streamlines, i.e. $W^u_{1D}(\boldsymbol{f}_{\mathcal{P},1,2})$, means that the partitioning is not strict;

https://doi.org/10.1017/jfm.2017.680 Published online by Cambridge University Press

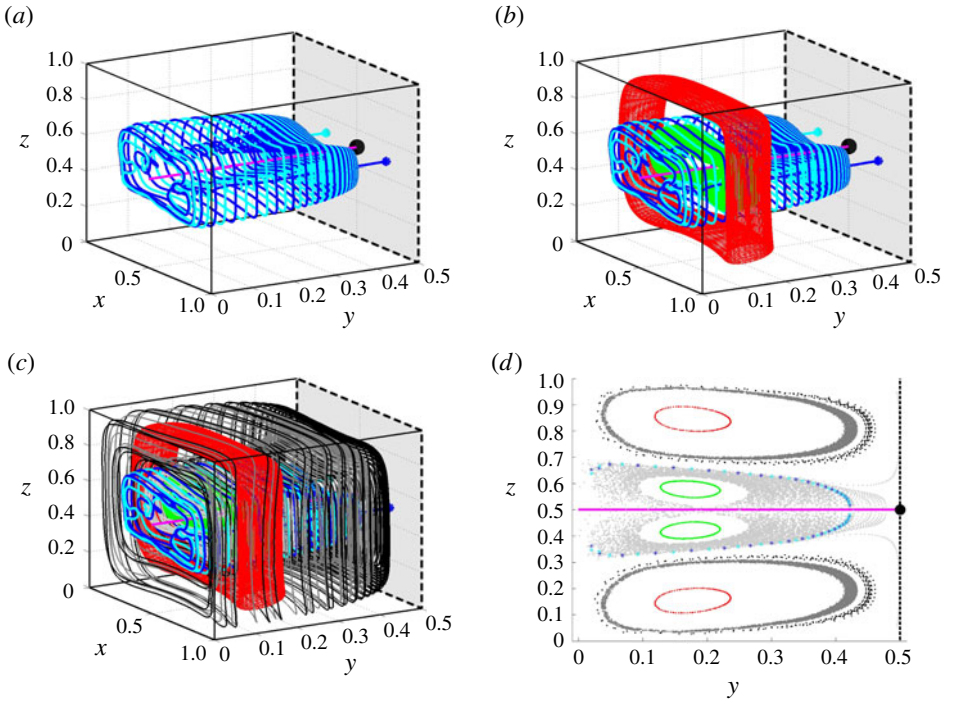



FIGURE 12. (Colour online) Typical bifurcated 3D flow topology in subregion $0 \leqslant y \leqslant 1/2$ separated by $\mathcal{P}$ (dashed/shaded) demonstrated for $Pr = 7$ and $Gr = 2.5 \times 10^4$: (*a*) formation of 'skeleton' by $W^u_{1D}(\boldsymbol{f}_{\mathcal{P},1,2})$ (blue/cyan) centred on $\mathcal{L}$ (magenta) partitioning shown subregion into interior and exterior zones; (*b*) interior (green) and exterior (red) families of KAM tori separated by 'skeleton'; (*c*) interior (light grey) and exterior (dark grey/black) chaotic streamlines; (*d*) Poincaré section $x = 1/2$ (shows larger portion of chaotic streamlines than in panel *c*.)

transport across this entity is possible yet severely impeded. Hence, the skeleton defines a porous transport barrier reminiscent of cantori (MacKay, Meiss & Percival 1984) and typically restricts tracers to one zone for prolonged periods of time. This is demonstrated in figure 11(*d*) by the Poincaré sections of streamlines belonging to $W^u_{2D}(\boldsymbol{n}_{\mathcal{P}})$ (black markers) and $W^u_{1D}(\boldsymbol{n}_{\mathcal{L}})$ (red markers). Both streamlines remain trapped in the skeleton proximity for a substantial time, yet eventually 'escape' near $\mathcal{P}$ (dashed line) into the exterior zone. (Note that the 'reversed-flow' streamlines adjacent to symmetry plane $\mathcal{P}$ in Mallinson & de Vahl Davis (1977) closely resemble $W^u_{1D}(\boldsymbol{f}_{\mathcal{P},1,2})$, lending credence to the earlier remark in § 4.2 that they likely belong to the above-mentioned chaotic region.)

The skeleton region originates from intricate manifold interactions corresponding with isolated stagnation points and, given the Hamiltonian structure of the Lagrangian equations of motion (§ 3.4) breaks down near such points (Bajer 1994), accommodates essentially 3D non-Hamiltonian dynamics. The Lagrangian behaviour within the zones interior and exterior to the skeleton, on the other hand, retains its Hamiltonian nature and thus is essentially similar to that in the inertia-dominated regime shown in figure 7. The flow topology in each zone namely consists of a single family of KAM tori centred on $\mathcal{L}$, *viz.* said primary (exterior) and secondary (interior) tori, of which one specimen is highlighted in green and red, respectively, in figure 12(*b*), and island

https://doi.org/10.1017/jfm.2017.680 Published online by Cambridge University Press

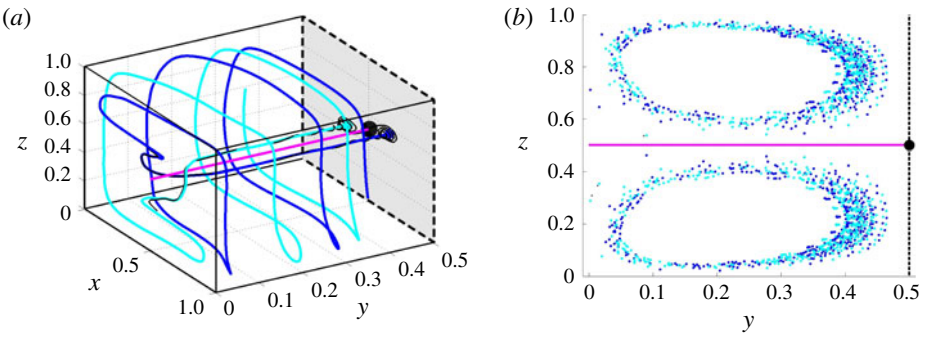



FIGURE 13. (Colour online) Bifurcated 3D flow topology in subregion $0 \leqslant y \leqslant 1/2$ separated by $\mathcal{P}$ (dashed/shaded) for $Pr = 0.71$ and $Gr = 7.2 \times 10^4$: (*a*) formation of 'skeleton' by $W^s_{1D}(\boldsymbol{f}_{\mathcal{P},1,2})$ (blue/cyan) centred on $\mathcal{L}$ (magenta) and encircled by a single streamline within $W^s_{2D}(\boldsymbol{n}_{\mathcal{P}})$ (black); (*b*) Poincaré section $x = 1/2$ (shows larger portion of streamlines than in panel *a*.)

chains (not shown). These coherent structures, in turn, are surrounded by chaotic streamlines, with one interior and two exterior specimens indicated in light grey and black/dark grey, respectively, in figure 12(*c*). The corresponding Poincaré section is given in figure 12(*d*) and exposes the full topological make-up. (The 3D perspective shows only part of the chaotic streamlines for reasons of legibility.) The interior chaotic streamline further demonstrates the nature and impact of the skeleton on the Lagrangian dynamics by remaining confined to this zone for a prolonged period of time before eventually 'escaping' into the chaotic region of the exterior zone. Note that the relatively denser winding of the exterior chaotic streamlines indicates a lower intensity in chaotic dynamics compared to the interior zone.

Examination of the post-bifurcation topologies for $Pr = (20, 50, 100)$ reveals essentially the same behaviour as above for $Pr = 7$. Secondary tori appear near bounding wall $y = 0$ and gradually expand towards symmetry plane $\mathcal{P}$ with increasing $Gr$ in the way demonstrated in figure 9. The concurrent emergence of stagnation points on symmetry line $\mathcal{L}$ implies that similar heteroclinic manifold interactions underlie the 3D flow topology. Hence, case $Pr = 7$ indeed is typical of the behaviour for 'larger' $Pr$.

### 5.3. *Absence of secondary tori (fluids with 'smaller' Pr)*

A typical bifurcated 3D flow topology without secondary tori occurring for 'smaller' $Pr$ (i.e. $Pr < Pr^*$) is demonstrated below for $Pr = 0.71$ and $Gr = 7.2 \times 10^4$. The skeleton defined by the 1D manifolds of the foci $\boldsymbol{f}_{\mathcal{P},1,2}$ emerging from symmetry plane $\mathcal{P}$ remains a key entity in the bifurcated flow topology in the case stagnation points on $\mathcal{L}$ are absent yet its extent and impact change significantly relative to the above. Figure 13(*a*), for example, shows said 1D manifolds (blue/cyan) for $Pr = 0.71$ and $Gr = 7.2 \times 10^4$ in conjunction with $\mathcal{L}$ (magenta) and a single streamline within the 2D manifold of $\boldsymbol{n}_{\mathcal{P}}$ (black). (Note that this concerns original stability of the saddle-foci arrangement, i.e. $W^s_{1D}(\boldsymbol{f}_{\mathcal{P},1,2})$ and $W^s_{2D}(\boldsymbol{n}_{\mathcal{P}})$; this is of secondary importance for the global 3D Lagrangian dynamics for reasons mentioned before.) Manifolds $W^s_{1D}(\boldsymbol{f}_{\mathcal{P},1,2})$ again describe a cocoon-like skeleton and act as 'centres' about which $W^s_{2D}(\boldsymbol{n}_{\mathcal{P}})$ progressively coils up. However, unlike the 'larger'-$Pr$ case, here the skeleton is far

https://doi.org/10.1017/jfm.2017.680 Published online by Cambridge University Press

more erratic and spread-out, as visualised by the corresponding Poincaré section in figure 13(b). Hence, the skeleton demarcates a large-scale chaotic region enveloping the single family of KAM tori and island chains shown in figure 4(c) instead of a cantorus-like transport barrier that effectively partitions the domain into zones with primary and secondary tori. Thus absence of stagnation points on $\mathcal{L}$ yields a bifurcated flow topology that, consistent with the tendency towards inertia-dominated dynamics for 'smaller' $Pr$ (§ 4.3), closely resembles the pre-bifurcation state $Gr < Gr^*$ (§ 4.1). An essential difference with the latter is that here the chaotic region, besides Hamiltonian chaos connected with breakdown of KAM tori, furthermore involves non-Hamiltonian chaos due to the manifolds associated with stagnation points within $\mathcal{P}$.

## 6. Conclusions

The present study concerns the Lagrangian dynamics of three-dimensional (3D) buoyancy-driven cavity flows under steady and laminar conditions due to a global temperature gradient imposed via an opposite hot and cold sidewall. This serves as the archetypal configuration for natural-convection flows in which (contrary to the well-known Rayleigh–Bénard flow) gravity is perpendicular (instead of parallel) to the global temperature gradient. Limited insight into the Lagrangian properties of this class of flows, despite its relevance to observed flow phenomena as well as scalar transport, motivates this study. The Lagrangian dynamics are investigated in terms of the generic structure and associated transport properties of the global streamline pattern ('Lagrangian flow topology') by both theoretical and computational analyses. The main findings on this study are summarised below. Moreover, an outlook to follow-up research is provided.

Two fundamental states can be distinguished on the basis of Grashof number $Gr$: linear limit $Gr = 0$ and nonlinear regime $Gr > 0$. Former and latter states are characterised by closed and (generically) non-closed streamlines, respectively. Symmetries render the buoyancy-driven flows dynamically/topologically analogous to single-wall lid-driven cavity flows. This implies two fundamental similarities between both flow classes: (i) diffeomorphic Lagrangian flow topologies (at least under weakly nonlinear conditions); (ii) a (locally) Hamiltonian structure of the 3D Lagrangian equations of motion. This has the important consequence that the response of the flow topology in the nonlinear regime $Gr > 0$ (initially) follows the same universal Hamiltonian route as the single-wall lid-driven flows: coalescence of closed streamlines into two families of tori (separated by the symmetry plane midway between the adiabatic sidewalls) for 'small' $Gr > 0$ and their progressive disintegration into chaotic streamlines with growing $Gr$. The physical mechanism triggering this behaviour is symmetry breaking due to nonlinearities introduced by fluid inertia and convective heat transfer.

Fluid inertia is the prevailing symmetry-breaking mechanism for 'small' $Gr$ and thus explains the (initial) dynamic similarity with lid-driven flows upon progressively introducing nonlinearity from the linear limit $Gr = 0$. The corresponding global flow topology is governed by a single focus-type stagnation point; its 2D and 1D manifolds define the above separating symmetry plane and toroidal axis of the (disintegrating) tori, respectively. However, for sufficient $Gr$, convective heat transfer gives rise to significant asymmetry of the temperature field and, in consequence, the buoyancy force. This results in a buoyancy-induced pitchfork bifurcation of the flow topology within the symmetry plane from a single focus into a node/saddle/saddle (NSS) with

https://doi.org/10.1017/jfm.2017.680 Published online by Cambridge University Press

accompanying pair of foci upon exceeding a finite threshold for $Gr$. The pitchfork bifurcation underlies the emergence of 'secondary rolls' reported in numerous studies in the literature. Symmetries and topological invariance in conjunction with physical considerations regarding thermal/flow phenomena imply that, irrespective of $Pr$, the system always follows this scenario upon increasing $Gr$ from the linear limit $Gr = 0$. However, the bifurcation threshold for $Gr$ decreases with increasing $Pr$ due to a transition from inertia-dominated to buoyancy-dominated dynamics at 'small' and 'large' $Pr$, respectively.

The global impact of the bifurcation can be distinguished into two cases: bifurcated flow topologies with and without secondary tori emerging adjacent to the original ('primary') tori at the adiabatic sidewalls. This qualitatively depends on the Prandtl number $Pr$ in that former and latter case tend to correspond with 'larger' and 'smaller' $Pr$, respectively. Given the transition from inertia-dominated to buoyancy-dominated dynamics with increasing $Pr$, this designates secondary tori as a buoyancy-induced phenomenon that occurs upon exceeding a certain threshold for $Pr$. Such secondary tori have, to the best of our knowledge, not been explicitly reported before and intimately relate to the occurrence of stagnation points outside the above-mentioned symmetry plane. The global post-bifurcation flow topology closely resembles the pre-bifurcation state in the case such points are absent; the bifurcation of the focus into an NSS and foci only has a localised effect. Presence of such points, on the other hand, results in the formation of a cocoon-like 'skeleton' due to intricate heteroclinic manifold interactions of stagnation points within and outside the symmetry plane. This entity partitions the subregion on each side of said plane into a zone interior and exterior to the skeleton and constitutes the 'separatrix' between primary (exterior zone) and secondary (interior zone) tori.

The global 3D flow topology is 'shaped' by stagnation points in the symmetry plane/line and their manifold interactions. Hence, further investigation of these entities versus the system parameters by the adopted approach enables comprehensive (Lagrangian) characterisation of the flow and transport properties of 3D buoyancy-driven flows. The generality of the Lagrangian methodology admits essentially the same strategy for the natural counterpart to the current system, i.e. Rayleigh–Bénard flows, as well as more complex thermally driven flows involving, for example, magnetic or radiative effects (Borjini *et al.* 2008; Henry *et al.* 2008; Soucasse *et al.* 2014), buoyancy-driven flows in porous media (Sankar *et al.* 2011), double-diffusion flows (Sezai & Mohamad 1999), different thermal boundary conditions (Sheu *et al.* 2008), buoyancy effects in lid-driven flows (Shankar, Meleshko & Nikiforovich 2002) or inclination of the global temperature gradient relative to gravity (Torres *et al.* 2014, 2015). Proper parameterisation for smooth introduction of nonlinear effects and *a priori* designation of existence regions for stagnation points by symmetry analyses facilitates a tractable and systematic Lagrangian investigation via (solenoidal representations of) the velocity field in basically any of these systems. Extension of this ansatz to critical points in the fluid trajectories of unsteady flows (e.g. periodic points in time-periodic buoyancy-driven flows; Contreras *et al.* (2016*a*)) may shed light on outstanding issues such as the transition to unsteady 3D buoyancy-driven flow (Lappa 2010).

Dedicated laboratory experiments are imperative for exhaustive Lagrangian analyses on thermally driven flows and may be realised in two ways. First, exploitation of analogies between flow classes as, for example, the dynamic similarity of the pre-bifurcation buoyancy-driven flow with lid-driven cavity flows. This may, for example, enable investigation of Lagrangian properties of the pre-bifurcation regime

https://doi.org/10.1017/jfm.2017.680 Published online by Cambridge University Press

with advanced 3D Lagrangian measurement techniques as 3D Particle-Tracking Velocimetry (3DPTV) using (adapted versions of) the experimental set-up of Znaien *et al.* (2012), Wu *et al.* (2014). Second, integration of Lagrangian techniques as 3DPTV in experimental set-ups employed in, for example, Hiller *et al.* (1989, 1990), McKell *et al.* (1990), Kowalewski (1998), Juel *et al.* (1999, 2001), Pallares *et al.* (2001), Hof *et al.* (2004), Hof, Juel & Mullin (2005). Efforts to this effect are underway.

**Acknowledgements**

P.S.C. gratefully acknowledges financial support from Consejo Nacional de Ciencia y Tecnología (CONACYT). This work has benefited substantially from insightful comments of an anonymous referee on the non-dimensional parameterisation of the problem.

## Appendix A. Spectral representation of the velocity field

### A.1. *Projection of the velocity field on a divergence-free basis*

In this section we describe the transformation for obtaining a divergence-free representation of the COMSOL velocity field. Key to reliable Lagrangian tracking is a velocity field that satisfies the incompressibility constraint to a very high degree of precision. However, velocity fields simulated with commercial flow solvers such as COMSOL generically do not offer this precision. Basically two strategies exist to deal with this issue. First, treatment of the kinematic equation with a volume-preserving time integration scheme (instead of the Taylor–Galerkin scheme); second, treatment of the velocity prior to utilisation for Lagrangian transport studies. Here the latter course of action is pursued by identically enforcing the incompressibility constraint $\boldsymbol{\nabla}\cdot\boldsymbol{u}=0$ through evaluation of $u_x$ from $(u_y, u_z)$ via inversion of the $x$-wise spatial derivative:

$$D_x u_x = -F, \quad D_x = \frac{\partial}{\partial x}, \quad F = \frac{\partial u_y}{\partial y} + \frac{\partial u_z}{\partial z} \quad \Rightarrow \quad u_x = -D_x^{-1} F. \qquad (\mathrm{A}\,1a\text{–}c)$$

This embarks on expression of the velocity field in a Chebyshev expansion, i.e.

$$\boldsymbol{u}(\boldsymbol{x}) = \sum_{m=0}^{M}\sum_{n=0}^{N}\sum_{p=0}^{P}(\widetilde{\boldsymbol{u}}_{mnp}\phi_m(2x-1)\phi_n(2y-1))\phi_p(2z-1), \qquad (\mathrm{A}\,2)$$

with $\phi_k(.)$ the $k$th-order Chebyshev polynomial and $\widetilde{f}_{mnp}$ the associated Chebyshev spectrum (Canuto *et al.* 1988). The Chebyshev spectrum $\widetilde{\boldsymbol{u}}_{mnp}$ is evaluated via standard discrete Chebyshev transformation from the velocity field $\boldsymbol{u}(\boldsymbol{x}_{ijl})$ on the discrete grid $\boldsymbol{x}_{ijl}=(x_i, y_j, z_l)$ defined by the Gauss–Lobatto quadrature points (Canuto *et al.* 1988). To this end the simulated velocity field is interpolated from the COMSOL grid onto the spectral grid $\boldsymbol{x}_{ijl}$ by way of built-in MATLAB routines.

An important property of the Chebyshev expansion (A 2) in the current context is that spatial derivatives of the velocity components translate into algebraic relations between the associated Chebyshev spectra; for example, $u_x^{(1)} \equiv \partial u_x/\partial x$ becomes $\widetilde{\boldsymbol{u}}_x^{(1)} = \widetilde{\boldsymbol{D}}_x\widetilde{\boldsymbol{u}}_x$, with $\widetilde{\boldsymbol{u}}_x^{(1)}$ and $\widetilde{\boldsymbol{u}}_x$ the corresponding matrices with spectral coefficients and $\widetilde{\boldsymbol{D}}_x$ the matrix representing the $x$-wise derivative (Canuto *et al.* 1988). A key point is

https://doi.org/10.1017/jfm.2017.680 Published online by Cambridge University Press

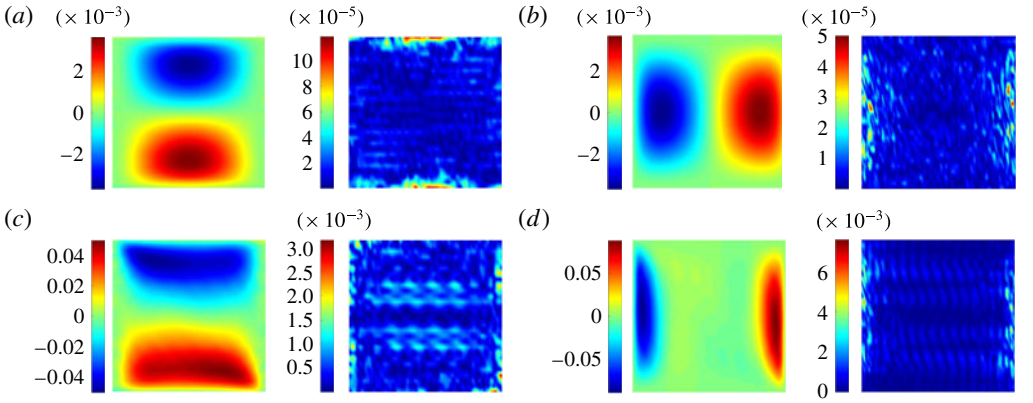



FIGURE 14. (Colour online) Spectral representation of the COMSOL field in terms of the planar field $(u_x, u_z)$ in the symmetry plane $\mathcal{P}$ for $M = N = P = 24$: (*a*) $u_x$ for $Gr = 0$; (*b*) $u_z$ for $Gr = 0$; (*c*) $u_x$ for $(Pr, Gr) = (7, 2.5 \times 10^4)$; (*d*) $u_z$ for $(Pr, Gr) = (7, 2.5 \times 10^4)$. Left and right maps in each panel correspond to the spectral representation and the deviation from the original COMSOL field, respectively.

that spectrum $\widetilde{\boldsymbol{u}}_x^{(1)}$ exactly represents the (spectrum of the) spatial derivative of the Chebyshev expansion of $u_x$ in any arbitrary position $\boldsymbol{x}$. This property holds equally for (the spatial derivatives of) $u_{y,z}$ and thus the spectral representation (A 2) enables exact transformation of the (inverted) differential equation (A 1) into the algebraic form

$$\widetilde{\boldsymbol{D}}_x\widetilde{\boldsymbol{u}}_x = -\widetilde{\boldsymbol{F}}, \quad \widetilde{\boldsymbol{F}} = \widetilde{\boldsymbol{D}}_y\widetilde{\boldsymbol{u}}_y + \widetilde{\boldsymbol{D}}_z\widetilde{\boldsymbol{u}}_z \quad \Rightarrow \quad \widetilde{\boldsymbol{u}}_x = -\widetilde{\boldsymbol{D}}_x^{-1}\widetilde{\boldsymbol{F}}, \tag{A 3a,b}$$

where $\widetilde{\boldsymbol{D}}_{y,z}$ correspond to the spatial derivatives in $(y, z)$-directions. This procedure determines $u_x$ up to an arbitrary contribution $\psi(y, z)$; any adjusted field $u_x' = u_x + \psi$ satisfies (A 3) as well. This ambiguity is readily eliminated by substituting mode $m = 0$, which corresponds to contributions to (A 2) of the form $\psi(y, z)$, by mode $m = 0$ of the untreated velocity component $u_x$ evaluated from Chebyshev transformation of the original COMSOL field.

The above yields the sought-after spectrum $\widetilde{\boldsymbol{u}}_x$ via standard linear algebra and gives a spectral representation (A 2) of $\boldsymbol{u}$ that satisfies $\boldsymbol{\nabla} \cdot \boldsymbol{u} = 0$ up to machine accuracy everywhere in the flow domain. Hence, employing (A 2) during numerical integration of the kinematic equation ensures, similar as in Speetjens & Clercx (2005), volume-preserving Lagrangian dynamics at all times. Figure 14 demonstrates the spectral representation in terms of the planar field $(u_x, u_z)$ in the symmetry plane $\mathcal{P}$ for the linear limit $Gr = 0$ (panels *a*,*b*) and the typical nonlinear case $(Pr, Gr) = (7, 2.5 \times 10^4)$ (panels *c*,*d*) using $M = N = P = 24$. (In this work we consider $M = N = P$ and for brevity only specify $M$.) Panels (*a*) and (*c*) give the spectral representation of component $u_x$ (left) and its deviation from the original COMSOL field (right); panels (*b*) and (*d*) give the accompanying results for component $u_z$. This reveals a close approximation of the original COMSOL field; deviations typically are several orders of magnitude below the velocity magnitude. Moreover, the spectral representation satisfies volume-preservation and symmetries in any arbitrary position $\boldsymbol{x}$ to machine precision.

https://doi.org/10.1017/jfm.2017.680 Published online by Cambridge University Press

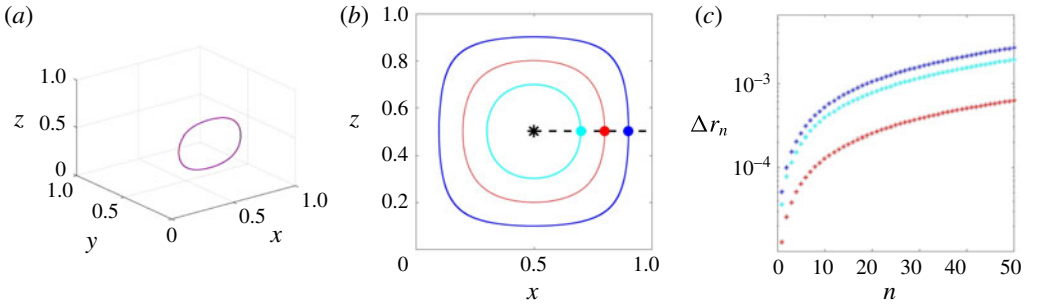



FIGURE 15. (Colour online) Performance of spectral Lagrangian tracking scheme for resolution of closed streamlines in limit $Gr = 0$: (*a*) typical streamline identified via COMSOL field (black) versus spectral representation ($M = 16$: blue; $M = 24$: magenta; $M = 36$: red); (*b*) streamlines in symmetry plane $\mathcal{P}$ (filled circles: initial tracer positions) determined with spectral approach ($M = 24$); (*c*) drift $\Delta r_n$ of intersection of streamlines with the horizontal axis (dashed in panel *b*) versus number of revolutions $n$ about the stagnation point (black star in panel *b*).

### A.2. *Performance of the spectral tracking algorithm*

A comparative analysis of the particle tracking using the COMSOL velocity field and its spectral representation for different orders of expansion is carried out. The first test cases concern limit $Gr = 0$ and 'small' $Gr$ following § 3.4, for which individual streamlines should, according to theory, describe a closed orbit and torus, respectively.

Figure 15(*a*) shows a typical single streamline for the limit $Gr = 0$ obtained by the dedicated spectral method for $M = (16, 24, 36)$ versus the standard tracking algorithm using the COMSOL field. The streamlines are virtually indistinguishable, signifying close agreement between both methods as well as convergence of the spectral representation. Moreover, the computed streamlines are closed to a high degree of precision, as demonstrated in figure 15(*b*) by way of three streamlines in symmetry plane $\mathcal{P}$ determined with the spectral approach for $M = 24$. The streamlines correspond with tracers released at initial positions $\boldsymbol{x}_0$ (filled circles) on the horizontal axis emerging from $\boldsymbol{x}_c$ (dashed) and tracked for 50 revolutions about the stagnation point $\boldsymbol{x}_c$ (black star). The subsequent windings of each streamline about $\boldsymbol{x}_c$ coincide to within $O(\Delta r_n)$, with $\Delta r_n = |\boldsymbol{x}_n - \boldsymbol{x}_0|$ the drift of the intersection of each streamline with said axis from its initial position after $n$ revolutions according to figure 15(*c*). The drift even after 50 revolutions is only of $O(10^{-3})$, meaning that the spectral method accurately resolves the closed streamlines and thus reliably captures the fundamental topological properties of limit $Gr = 0$.

Figure 16(*a*,*b*) give the 3D streamline and corresponding Poincaré section, respectively, for case $Pr = 0.71$ and $Gr = 3.2 \times 10^3$, which corresponds with the regime of 'small' $Gr$. This reveals that both the COMSOL and spectral approaches again perform consistently with theory by recovering a torus. Furthermore, structures again being indistinguishable implies that the chosen $M$ also here suffice for convergence of the spectral method. However, case $Gr = 3.2 \times 10^3$ exposes a crucial difference in performance between COMSOL and spectral approaches. The Poincaré section of the former exhibits a gradual drifting from a closed orbit (and thus a torus in 3D) for long integration times (not shown). This violates the Hamiltonian nature of the Lagrangian dynamics and must be attributed to computational departures from the incompressibility constraint by the standard approach (Speetjens & Clercx 2005).

https://doi.org/10.1017/jfm.2017.680 Published online by Cambridge University Press

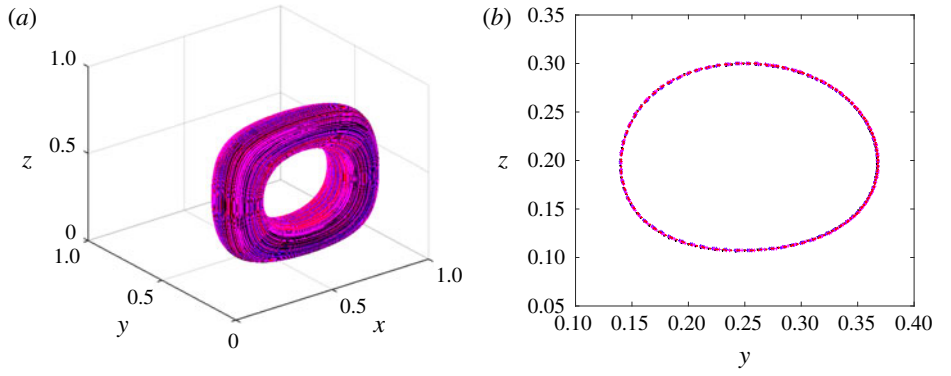



FIGURE 16. (Colour online) Performance of spectral Lagrangian tracking scheme for resolution of KAM tori for 'small' $Gr$ demonstrated by case $Pr = 0.71$ and $Gr = 3.2 \times 10^3$: (*a*) typical streamline delineating a KAM torus identified via COMSOL field (black) versus spectral representation ($M = 16$: blue; $M = 24$: magenta; $M = 36$: red); (*b*) corresponding Poincaré sections.

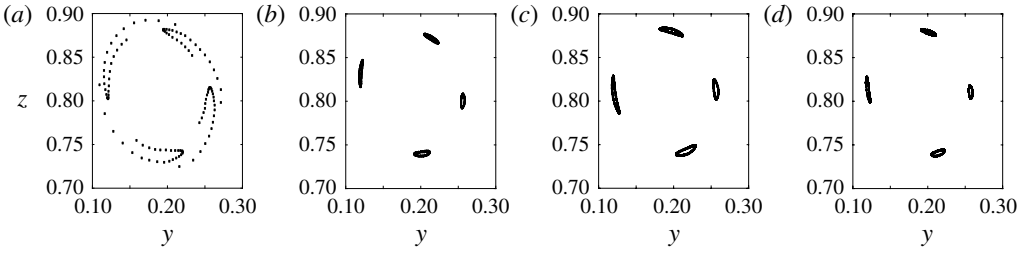



FIGURE 17. Performance of spectral Lagrangian tracking scheme for resolution of typical island chain at 'large' $Gr$ demonstrated by case $Pr = 0.71$ and $Gr = 7.2 \times 10^4$: (*a*) COMSOL; (*b–d*) spectral approach for $M = 16$ (*b*), $M = 24$ (*c*) and $M = 36$ (*d*).

The streamline following the spectral approach, on the other hand, remains closed, meaning this method is devoid of such numerical artefacts and thus outperforms the COMSOL approach for Lagrangian analyses.

A further test case concerns 'large' $Gr$ following § 3.4 and corresponds with complex Poincaré sections consisting of KAM tori and island chains embedded in chaotic seas. Figure 17 shows the Poincaré section of a typical island chain for $Pr = 0.71$ and $Gr = 7.2 \times 10^4$ obtained with the COMSOL approach (panel *a*) versus the spectral approach for $M$ as indicated (panels *b–d*). The COMSOL result exhibits substantial drifting from an island-chain structure for reasons given before, thus further consolidating the above finding of its inferior performance for Lagrangian analyses. The spectral results, in contrast, retain the same island structure – and thus are faithful to the Hamiltonian nature of the dynamics – for all $M$. The effect of $M$ is entirely quantitative in that the island chain shifts and deforms slightly with varying $M$. The results suggest that convergence requires a somewhat higher resolution (i.e. $M \gtrsim 24$) than in the regimes considered before.

Figure 18 gives the full Poincaré section for $Pr = 0.71$ and $Gr = 7.2 \times 10^4$ using the spectral approach versus $M$. This reveals that the topological composition is preserved for all $M$, and variations are again entirely quantitative and restricted to minor shifts

https://doi.org/10.1017/jfm.2017.680 Published online by Cambridge University Press

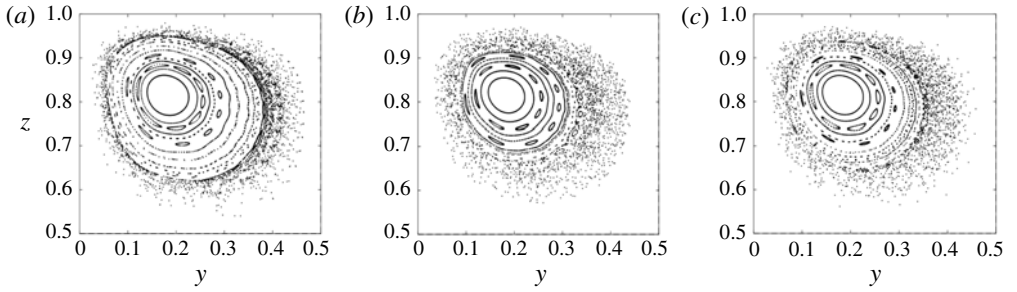



FIGURE 18. Performance of spectral Lagrangian tracking scheme for resolution of typical island chains within chaotic sea at 'large' $Gr$ demonstrated by case $Pr = 0.71$ and $Gr = 7.2 \times 10^4$: (*a*) $M = 16$; (*b*) $M = 24$; (*c*) $M = 36$.

and deformations; $M \gtrsim 24$ again emerges as adequate resolution for convergence. This further demonstrates the superior performance of the spectral approach for reliable Lagrangian analyses. Extensive testing for different $Pr$ and $Gr$ (not shown) confirmed these findings.

## Appendix B. Hamiltonian structure of the Lagrangian dynamics

The primary circulation, shown in § 3, causes the formation of two toroidal regions on either side of $\mathcal{P}$ (figure 2*e*). The interior of each such region is diffeomorphic to a unit torus. This advances a curvilinear reference frame $\boldsymbol{\xi} = (\xi_1, \xi_2, \xi_3)$ diffeomorphic to the toroidal reference frame associated with this unit torus. $(\xi_1, \xi_2)$ and $\xi_3$ are the (curvilinear counterparts to the) poloidal and toroidal coordinates, respectively, as a natural counterpart to the Cartesian frame $\boldsymbol{x} = (x, y, z)$. The transformation of the kinematic equation (2.2) is (formally) defined by

$$\frac{\mathrm{d}\boldsymbol{x}}{\mathrm{d}t} = \boldsymbol{u}(\boldsymbol{x}) \quad \Rightarrow \quad \frac{\mathrm{d}\boldsymbol{\xi}}{\mathrm{d}t} = \boldsymbol{v}(\boldsymbol{\xi}), \tag{B 1}$$

with $v_i = \boldsymbol{u} \cdot \boldsymbol{e}_i / h_i$ the curvilinear velocity components and $\boldsymbol{e}_i = h_i^{-1} \partial \boldsymbol{x} / \partial \xi_i$ and $h_i = |\partial \boldsymbol{x} / \partial \xi_i|$ the corresponding unit vectors and scaling factors, respectively (Arfken & Weber 2005). A key advantage of the curvilinear representation (B 1) is that it yields a flow with a uni-directional toroidal component $u_3 = \boldsymbol{u} \cdot \boldsymbol{e}_3 > 0$ everywhere inside the toroidal region. This admits subsequent transformation of the kinematic equation from the physical frame $\boldsymbol{\xi} = (\xi_1, \xi_2, \xi_3)$ to a canonical space–time frame $\boldsymbol{\zeta} = (\zeta_1, \zeta_2, \tau)$, i.e.

$$\frac{\mathrm{d}\boldsymbol{\xi}}{\mathrm{d}t} = \boldsymbol{v}(\boldsymbol{\xi}) \quad \Rightarrow \quad \left( \frac{\mathrm{d}\zeta_1}{\mathrm{d}\tau}, \frac{\mathrm{d}\zeta_2}{\mathrm{d}\tau} \right) = \left( \frac{\partial \mathcal{H}}{\partial \zeta_2}, -\frac{\partial \mathcal{H}}{\partial \zeta_1} \right), \tag{B 2}$$

where the (canonical) time $\tau$ is associated with the poloidal velocity component $u_3$. The transformation is according to Bajer (1994) and relies on the vector potential $\boldsymbol{A} = A_1 \boldsymbol{e}_1 + A_3 \boldsymbol{e}_3$ of the physical velocity $\boldsymbol{u}$, which is implicitly defined by

$$u_1 = \frac{1}{h_2 h_3} \frac{\partial}{\partial \xi_2} (h_3 A_3), \quad u_2 = \frac{1}{h_1 h_3} \left[ \frac{\partial}{\partial \xi_3} (h_1 A_1) - \frac{1}{h_2 h_3} \frac{\partial}{\partial \xi_1} (h_3 A_3) \right], \tag{B 3a,b}$$

$$u_3 = -\frac{1}{h_1 h_2} \frac{\partial}{\partial \xi_2} (h_1 A_1). \tag{B 4}$$

https://doi.org/10.1017/jfm.2017.680 Published online by Cambridge University Press

The transformation links the canonical space $(\zeta_1, \zeta_2)$, the canonical time $\tau$ and the Hamiltonian $\mathcal{H}$ with the curvilinear coordinates via

$$\zeta_1 = \xi_1, \quad \zeta_2 = -h_1(\boldsymbol{\xi})A_1(\boldsymbol{\xi}) = P(\xi_2; \xi_1, \xi_3), \quad \tau = \xi_3, \quad \mathcal{H}(\zeta_1, \zeta_2, \tau) = h_3 A_3|_{\boldsymbol{\xi}(\zeta_1,\zeta_2,\tau)}, \tag{B 5$a$–$d$}$$

where $P$ effectively is a function parameterised by $(\xi_1, \xi_3)$ that nonlinearly relates the canonical coordinate $\zeta_2$ and the curvilinear coordinate $\xi_2$. Hence, the physical space and the canonical space–time domain coincide, save for a nonlinear 'deformation' in the $\xi_2$-direction. Transformation (A 5) exists everywhere outside stagnation points (Bajer 1994). The latter are absent in the primary circulation, implying that the kinematic equation (2.2), and thus the Lagrangian dynamics, indeed has an intrinsic Hamiltonian structure. Refer to Speetjens *et al.* (2014) for an intimately related transformation for periodic duct flows (which are also topologically toroidal domains).

Any cross-section $\mathcal{A}$ transverse to the $\xi_3$-direction effectively is a 'snapshot' in the canonical time $\tau$ of the 2D Hamiltonian system in the canonical space $(\zeta_1, \zeta_2)$. The primary circulation causes streamlines to systematically return to such a cross-section and thus produces consecutive 'snapshots' of the 2D Hamiltonian system. This admits the definition of a map $\boldsymbol{x}_{k+1} = \boldsymbol{\Phi}(\boldsymbol{x}_k)$ that describes the 'snapshot-wise' evolution of the Lagrangian positions $\boldsymbol{x} = (x_1, x_2)$ within $\mathcal{A}$ in a manner essentially equivalent to the stroboscopic map of a 2D time-periodic system.

## REFERENCES


Aref, H. 2002 The development of chaotic advection. *Phys. Fluids* **14** (4), 1315–1325.

Aref, H., Blake, J. R., Budišić, M., Cardoso, S. S. S., Cartwright, J. H. E., Clercx, H. J. H., Feudel, U., Golestanian, R., Gouillart, E., Le Guer, Y. *et al.* 2017 Frontiers of chaotic advection. *Rev. Mod. Phys.* **89**, 025007.

Arfken, G. B. & Weber, H. J. 2005 *Mathematical Methods for Physicists*. Elsevier.

Arnol'd, V. I. 1989 *Mathematical Methods of Classical Mechanics*. Springer.

Awbi, H. B. 2008 *Ventilation Systems: Design and Performance*. Taylor & Francis.

Bajer, K. 1994 Hamiltonian formulation of the equations of streamlines in three-dimensional steady flows. *Chaos Solitons Fractals* **4** (6), 895–911.

Batchelor, G. K. 1954 Heat transfer by free convection across a closed cavity between vertical boundaries at different temperatures. *Q. Appl. Maths* **12** (3), 209–233.

Bejan, A. 2013 *Convection Heat Transfer*. Wiley.

Bennett, B., Anne, V. & Hsueh, J. 2006 Natural convection in a cubic cavity: implicit numerical solution of two benchmark problems. *Numer. Heat Transfer* A **50** (2), 99–123.

Bird, R. B., Stewart, W. E. & Lightfoot, E. N. 2007 *Transport Phenomena*. Wiley.

Borjini, M. N., Aissia, H. B., Halouani, K. & Zeghmati, B. 2008 Effect of radiative heat transfer on the three-dimensional buoyancy flow in cubic enclosure heated from the side. *Intl J. Heat Fluid Flow* **29** (1), 107–118.

Brouwer, L. E. J. 1911 Über Abbildung von Mannigfaltigkeiten. *Math. Ann.* **71**, 97–115.

Canuto, C., Hussaini, M. Y., Quarteroni, A. & Zang, T. A. 1988 *Spectral Methods in Fluid Dynamics*. Springer.

Cartwright, J. H. E., Feingold, M. & Piro, O. 1996 Chaotic advection in three-dimensional unsteady incompressible laminar flow. *J. Fluid Mech.* **316**, 259–284.

Cheng, C. Q. & Sun, Y. S. 1990*a* Existence of invariant tori in three-dimensional measure preserving mappings. *Celest. Mech.* **47**, 275–292.

Cheng, C. Q. & Sun, Y. S. 1990*b* Existence of periodically invariant curves in three-dimensional measure-preserving mappings. *Celest. Mech.* **47**, 293–303.


https://doi.org/10.1017/jfm.2017.680 Published online by Cambridge University Press

CHONG, M. S., PERRY, A. E. & CANTWELL, B. J. 1990 A general classification of three-dimensional flow fields. *Phys. Fluids* A **2**, 765–777.

CONTRERAS, P. S., DE LA CRUZ, L. M. & RAMOS, E. 2016*a* Topological analysis of a mixing flow generated by natural convection. *Phys. Fluids* **28** (1), 013602.

CONTRERAS, P. S., SPEETJENS, M. F. M. & CLERCX, H. J. H. 2016*b* Buoyancy-induced Lagrangian chaos: the differentially-heated cavity revisited. *J. Phys. Conf. Ser.* **745** (3), 032039.

DAVIES, G. F. 2011 *Mantle Convection for Geologists*. Cambridge University Press.

ELDER, J. W. 1965 Laminar free convection in a vertical slot. *J. Fluid Mech.* **23** (1), 77–98.

FRANJIONE, J. G. & OTTINO, J. M. 1992 Symmetry concepts for the geometric analysis of mixing flows. *Proc. R. Soc. Lond.* A **338** (1650), 301–323.

GETLING, A. V. 1998 *Rayleigh–Bénard Convection: Structures and Dynamics*. World Scientific.

GIAIOTTI, D. B., STEINACKER, R. & STEL, F. 2007 *Atmospheric Convection: Research and Operational Forecasting Aspects*. Springer.

GILL, A. E. 1966 The boundary-layer regime for convection in a rectangular cavity. *J. Fluid Mech.* **26** (3), 515–536.

GUCKENHEIMER, J. & HOLMES, P. 1983 *Nonlinear Oscillations, Dynamical Systems and Bifurcations of Vector Fields*. Springer.

HENKES, R. A. W. M. & HOOGENDOORN, C. J. 1990 On the stability of the natural convection flow in a square cavity heated from the side. *Appl. Sci. Res.* **47** (3), 195–220.

HENLE, M. 1979 *A Combinatorial Introduction to Topology*. Freeman.

HENRY, D. & BENHADID, H. 2007 Multiple flow transitions in a box heated from the side in low-Prandtl-number fluids. *Phys. Rev.* E **76**, 016314.

HENRY, D. & BUFFAT, M. 1998 Two-and three-dimensional numerical simulations of the transition to oscillatory convection in low-Prandtl-number fluids. *J. Fluid Mech.* **374**, 145–171.

HENRY, D., JUEL, A., BEN HADID, H. & KADDECHE, S. 2008 Directional effect of a magnetic field on oscillatory low-Prandtl-number convection. *Phys. Fluids* **20** (3), 034104.

HILLER, W. J., KOCH, ST. & KOWALEWSKI, T. A. 1989 Three-dimensional structures in laminar natural convection in a cubic enclosure. *Exp. Therm. Fluid Sci.* **2** (1), 34–44.

HILLER, W. J., KOCH, ST., KOWALEWSKI, T. A., DE VAHL DAVIS, G. & BEHNIA, M. 1990 Experimental and numerical investigation of natural convection in a cube with two heated side walls. In *Proceedings of IUTAM Symposium, Cambridge, UK August 13-18, 1989* (ed. K. Moffatt & A. Tsinober), pp. 717–726. Cambridge University Press.

HOF, B., JUEL, A. & MULLIN, T. 2005 Magnetohydrodynamic damping of oscillations in low-Prandtl-number convection. *J. Fluid Mech.* **545**, 193–201.

HOF, B., JUEL, A., ZHAO, L., HENRY, D., BEN HADID, H. & MULLIN, T. 2004 On the onset of oscillatory convection in molten gallium. *J. Fluid Mech.* **515**, 391–413.

ISHII, K., OTA, C. & ADACHI, S. 2012 Streamlines near a closed curve and chaotic streamlines in steady cavity flows. *Procedia IUTAM* **5**, 173–186.

JUEL, A., MULLIN, T., BEN HADID, H. & HENRY, D. 1999 Magnetohydrodynamic convection in molten gallium. *J. Fluid Mech.* **378**, 97–118.

JUEL, A., MULLIN, T., BEN HADID, H. & HENRY, D. 2001 Three-dimensional free convection in molten gallium. *J. Fluid Mech.* **436**, 267–281.

KELMANSON, M. A. & LONSDALE, B. 1996 Eddy genesis in the double-lid-driven cavity. *Q. J. Mech. Appl. Maths* **49** (4), 635–655.

KOWALEWSKI, T. A. 1998 Experimental validation of numerical codes in thermally driven flows. In *In Adv. Comput. Heat Transfer*, pp. 1–15. Begel House Inc.

LABROSSE, G., TRIC, E., KHALLOUF, H. & BETROUNI, M. 1997 A direct (pseudo-spectral) solver of the 2D/3D Stokes problem: Transition to unsteadiness of natural-convection flow in a differentially heated cubical cavity. *Numer. Heat Transfer* B **31** (3), 261–276.

LAPPA, M. 2010 *Thermal Convection: Patterns, Evolution and Stability*. Wiley.

LAURE, P. 1987 Study on convective motions in a rectangular cavity with a horizontal gradient of temperature. *J. Méc. Théor. Appl.* **6** (3), 351–382.

MACKAY, R. S., MEISS, J. D. & PERCIVAL, I. C. 1984 Stochasticity and transport in hamiltonian systems. *Phys. Rev. Lett.* **52**, 697.

https://doi.org/10.1017/jfm.2017.680 Published online by Cambridge University Press

MALLINSON, G. D. & DE VAHL DAVIS, G. 1973 The method of the false transient for the solution of coupled elliptic equations. *J. Comput. Phys.* **12** (4), 435–461.

MALLINSON, G. D. & DE VAHL DAVIS, G. 1977 Three-dimensional natural convection in a box: a numerical study. *J. Fluid Mech.* **83** (01), 1–31.

MARKATOS, N. C. & PERICLEOUS, K. A. 1984 Laminar and turbulent natural convection in an enclosed cavity. *Intl J. Heat Mass Transfer* **27** (5), 755–772.

MCKELL, K. E., BROOMHEAD, D. S., JONES, R. & HURLE, D. T. J. 1990 Torus doubling in convecting molten gallium. *Europhys. Lett.* **12** (6), 513.

MEISS, J. D. 2015 Thirty years of turnstiles and transport. *Chaos* **25** (9), 097602.

MELNIKOV, D. E. & SHEVTSOVA, V. M. 2005 Liquid particles tracing in three-dimensional buoyancy-driven flows. *Fluid Dyn. Mater. Process.* **1**, 189–199.

MERCADER, I., BATISTE, O., RAMÍREZ-PISCINA, L., RUIZ, X., RÜDIGER, S. & CASADEMUNT, J. 2005 Bifurcations and chaos in single-roll natural convection with low Prandtl number. *Phys. Fluids* **17** (10), 104108.

METCALFE, G., SPEETJENS, M. F. M., LESTER, D. R. & CLERCX, H. J. H. 2012 Beyond passive: Chaotic transport in stirred fluids. In *Advances in Applied Mechanics* (ed. E. van der Giessen & H. Aref), vol. 45, pp. 109–188. Elsevier.

MOHARANA, N. R., SPEETJENS, M. F. M., TRIELING, R. R. & CLERCX, H. J. H. 2013 Three-dimensional Lagrangian transport phenomena in unsteady laminar flows driven by a rotating sphere. *Phys. Fluids* **25** (9), 093602.

NIELD, D. A. & BEJAN, A. 2006 *Convection in Porous Media*. Springer.

OSTRACH, S. 1972 Natural convection in enclosures. *Adv. Heat Transfer* **8**, 161–227.

OSTRACH, S. 1988 Natural convection in enclosures. *Trans. ASME J. Heat Transfer* **110**, 1175–1190.

OTESKI, L., DUGUET, Y. & PASTUR, L. R. 2014 Lagrangian chaos in confined two-dimensional oscillatory convection. *J. Fluid Mech.* **759**, 489–519.

OTESKI, L., DUGUET, Y., PASTUR, L. R. & LE QUÉRÉ, P. 2015 Quasiperiodic routes to chaos in confined two-dimensional differential convection. *Phys. Rev.* E **92** (4), 043020.

OTT, E. 2002 *Chaos in Dynamical Systems*. Cambridge University Press.

PALLARES, J., ARROYO, M. P., GRAU, F. X. & GIRALT, F. 2001 Experimental laminar Rayleigh–Bénard convection in a cubical cavity at moderate Rayleigh and Prandtl numbers. *Exp. Fluids* **31** (2), 208–218.

PHILLIPS, T. N. 1984 Natural convection in an enclosed cavity. *J. Comput. Phys.* **54** (3), 365–381.

SANKAR, M., BHUVANESWARI, M., SIVASANKARAN, S. & DO, Y. 2011 Buoyancy induced convection in a porous cavity with partially thermally active sidewalls. *Intl J. Heat Mass Transfer* **54** (25), 5173–5182.

SEZAI, I. & MOHAMAD, A. A. 1999 Three-dimensional double-diffusive convection in a porous cubic enclosure due to opposing gradients of temperature and concentration. *J. Fluid Mech.* **400**, 333–353.

SHANKAR, P. N. 1997 Three-dimensional eddy structure in a cylindrical container. *J. Fluid Mech.* **342**, 97–118.

SHANKAR, P. N. 1998 Three-dimensional Stokes flow in a cylindrical container. *Phys. Fluids* **10** (3), 540–549.

SHANKAR, P. N. & DESHPANDE, M. D. 2000 Fluid mechanics in the driven cavity. *Annu. Rev. Fluid Mech.* **32**, 93–136.

SHANKAR, P. N., MELESHKO, V. V. & NIKIFOROVICH, E. I. 2002 Slow mixed convection in rectangular containers. *J. Fluid Mech.* **471**, 203–217.

SHEU, T. W. H., RANI, H. P., TAN, T.-C. & TSAI, S. F. 2008 Multiple states, topology and bifurcations of natural convection in a cubical cavity. *Comput. Fluids* **37** (8), 1011–1028.

SOUCASSE, L., RIVIÈRE, P., SOUFIANI, A., XIN, S. & LE QUÉRÉ, P. 2014 Transitional regimes of natural convection in a differentially heated cubical cavity under the effects of wall and molecular gas radiation. *Phys. Fluids* **26** (2), 024105.

SPEETJENS, M. F. M. & CLERCX, H. J. H. 2005 A spectral solver for the Navier–Stokes equations in the velocity–vorticity formulation. *Intl J. Comput. Fluid Dyn.* **19** (3), 191–209.

https://doi.org/10.1017/jfm.2017.680 Published online by Cambridge University Press

SPEETJENS, M. F. M. & CLERCX, H. J. H. 2013 Formation of coherent structures in a class of realistic 3D unsteady flows. In *Fluid Dynamics in Physics, Engineering and Environmental Applications* (ed. J. Klapp *et al.*), pp. 139–157. Springer.

SPEETJENS, M. F. M., CLERCX, H. J. H. & VAN HEIJST, G. J. F. 2004 A numerical and experimental study on advection in three-dimensional Stokes flows. *J. Fluid Mech.* **514**, 77–105.

SPEETJENS, M. F. M., CLERCX, H. J. H. & VAN HEIJST, G. J. F. 2006 Merger of coherent structures in time-periodic viscous flows. *Chaos* **16** (4), 043104,1–8.

SPEETJENS, M. F. M., DEMISSIE, E. A., METCALFE, G. & CLERCX, H. J. H. 2014 Lagrangian transport characteristics of a class of three-dimensional inline-mixing flows with fluid inertia. *Phys. Fluids* **26**, 113601.

TORRES, J. F., HENRY, D., KOMIYA, A. & MARUYAMA, S. 2014 Bifurcation analysis of steady natural convection in a tilted cubical cavity with adiabatic sidewalls. *J. Fluid Mech.* **756**, 650–688.

TORRES, J. F., HENRY, D., KOMIYA, A. & MARUYAMA, S. 2015 Transition from multiplicity to singularity of steady natural convection in a tilted cubical enclosure. *Phys. Rev.* E **92** (2), 023031.

TURCOTTE, D. L. & SCHUBERT, G. 2002 *Geodynamics*. Cambridge University Press.

DE VAHL DAVIS, G. 1968 Laminar natural convection in an enclosed rectangular cavity. *Intl J. Heat Mass Transfer* **11** (11), 1675–1693.

DE VAHL DAVIS, G. 1983 Natural convection of air in a square cavity: a bench mark numerical solution. *Intl J. Numer. Meth. Fluids* **3** (3), 249–264.

WAKASHIMA, S. & SAITOH, T. S. 2004 Benchmark solutions for natural convection in a cubic cavity using the high-order time–space method. *Intl J. Heat Mass Transfer* **47** (4), 853–864.

WU, F., SPEETJENS, M. F. M., VAINCHTEIN, D. L., TRIELING, R. R. & CLERCX, H. J. H. 2014 Comparative numerical-experimental analysis of the universal impact of arbitrary perturbations on transport in three-dimensional unsteady flows. *Phys. Rev.* E **90** (6), 063002.

YARIN, A. L., KOWALEWSKI, T. A., HILLER, W. J. & KOCH, ST. 1996 Distribution of particles suspended in convective flow in differentially heated cavity. *Phys. Fluids* **8** (5), 1130–1140.

ZNAIEN, J., SPEETJENS, M. F. M., TRIELING, R. R. & CLERCX, H. J. H. 2012 Observability of periodic lines in three-dimensional lid-driven cylindrical cavity flows. *Phys. Rev.* E **85** (6), 066320.

https://doi.org/10.1017/jfm.2017.680 Published online by Cambridge University Press